HHS Public Access

Author manuscript

Biomaterials. Author manuscript; available in PMC 2019 February 01.

Published in final edited form as:

Biomaterials. 2018 February ; 155: 217–235. doi:10.1016/j.biomaterials.2017.11.025.

Recent Progress on Semiconducting Polymer Nanoparticles for Molecular Imaging and Cancer Phototherapy

Jingchao Li[a], **Jianghong Rao**[b], and **Kanyi Pu**[a]

[a]School of Chemical and Biomedical Engineering, Nanyang Technological University, 70 Nanyang Drive, 637457, Singapore

[b]Molecular Imaging Program at Stanford, Departments of Radiology and Chemistry, Stanford University, 1201 Welch Road, Stanford, CA 94305-5484 (USA)

Abstract

As a new class of organic optical nanomaterials, semiconducting polymer nanoparticles (SPNs) have the advantages of excellent optical properties, high photostability and facile surface functionalization, and are considered to possess good biocompatibility for biomedical applications. This review surveys recent progress made on the design and synthesis of SPNs for molecular imaging and cancer phototherapy. A variety of novel polymer design, chemical modification and nanoengineering strategies have been developed to precisely tune up optoelectronic properties of SPNs to enable fluorescence, chemiluminescence and photoacoustic (PA) imaging in living animals. With these imaging modalities, SPNs have been demonstrated not only to image tissues such as lymph nodes, vascular structure and tumors, but also to detect disease biomarkers such as reactive oxygen species (ROS) and protein sulfenic acid as well as physiological indexes such as pH and blood glucose concentration. The potentials of SPNs in cancer phototherapy including photodynamic and photothermal therapy are also highlighted with recent examples. Future efforts should further expand the use of SPNs in biomedical research and may even move them beyond pre-clinical studies.

Keywords

Semiconducting polymer nanoparticles; photoacoustic imaging; molecular imaging; phototherapy; cancer therapy

1. Introduction

The integration of nanotechnology with healthcare has led to the application of nanoparticles in medicine and received more and more attention over the last two decades [1–4]. Owing to the unique properties including small size, large surface area, and ideal *in vivo* kinetics, nanoparticles can provide many benefits and new opportunities to address various life-threatening diseases [5]. The potential utility of nanoparticles as delivery vehicles for therapeutic agents has been demonstrated [6–9]. Nanoparticles can also serve as imaging agents, allowing for detection of biomarkers and cellular functions at disease site [10–13]. Many approaches have been developed to increase the *in vivo* colloidal stability, prolong the blood circulation time, improve the excretion rate from bodies, or enhance the accumulation

in lesion tissues [14]. The current data prove the promise of nanoparticles in pre-clinical and clinical applications.

Both inorganic and organic nanoparticles have been exploited for medicine [15–18]. Among them, semiconducting polymer nanoparticles (SPNs) are considered as one of the most attractive candidates because of their excellent optical properties [19–21]. SPNs are mainly composed of hydrophobic but optically and electronically active semiconducting polymers (SPs) and amphiphilic polymer matrixes (optional) [22, 23]. The optical properties of SPNs are mainly determined by the molecular structures of SPs [24–26]. Thereby, the absorption coefficients and photostability of SPNs are relatively higher as compared to small molecule dyes and their assembled supramolecular nanoparticles [27, 28]. Furthermore, SPNs are completely organic and biologically inert, and thus intrinsically circumvent the issue of heavy metal ion-induced toxicity to living organisms [29, 30]. All these features make SPNs highly promising for many biological applications, which include sensing of pH, ions and temperature [31–34], molecular imaging of tissues, disease biomarkers and physiological indexes [35–39], photothermal ablation of tumors [40–42], real-time activation of neurons [43] as well as photodynamic therapy of cancers and microorganisms [44, 45].

The optical properties, synthetic method, *in vivo* biocompatibility and biological applications of SPNs have been summarized in a number of recent reviews [46–53]. This review mainly reports the recent progress on the development of SPNs for molecular imaging and phototherapy in living animals. Chemical structures of SPs, semiconducting oligomers (SOs) and amphiphilic polymers used for preparation of these SPNs are summarized in Schemes 1–3, respectively. The *in vivo* applications of SPNs for fluorescence, chemiluminescence and photoacoustic (PA) imaging of different biological systems including tissues, disease biomarkers and physiological indexes are first introduced in details. Then the feasibility to use SPNs as therapeutic agents for photothermal and photodynamic therapy of cancers is also discussed. At last, a brief conclusion is given along with the discussion of current challenges and perspectives.

2. Preparation of SPNs

Current approaches to prepare SPNs mainly rely on mini-emulsion and nanoprecipitation methods [28]. As for mini-emulsion, SPs are dissolved in a water-immiscible organic solvent such as dichloromethane and then mixed with an aqueous solution containing appropriate surfactants under ultrasonication or vigorous stirring to form oil-in-water droplets. SPNs suspended in water are obtained after evaporation of organic solvent (Scheme 4a). To prepare SPNs through nanoprecipitation, SPs and amphiphilic polymers (optional) are dissolved in a water-miscible organic solvent such as tetrahydrofuran (THF), and the resulted solution is then quickly injected into water under ultrasonication. After nanoprecipitation occurs, organic solvent is removed to afford water dispersible SPNs (Scheme 4b). The different approaches have some influence on the diameters of SPNs. In general, mini-emulsion produces lager nanoparticles with a diameter ranging from 40-500 nm, while nanoprecipitation often gives smaller SPNs (5-50 nm) [22]. If surfactants or amphiphilic polymers are used, a high yield of SPNs can be achieved, close to 100% [54].

Additionally, most of the used SPs, surfactants, amphiphilic polymers and organic solvent are commercially available, enabling the large-scale preparation of SPNs.

3. Fluorescence imaging

SPNs represent a new class of fluorescent nanomaterials with exceptional brightness and good photostability [50, 55–59]. The application of SPNs as fluorescent probes for molecular imaging and sensing both *in vitro* and *in vivo* have been widely reported [56, 60–62]. Modification of SPNs with ligands or biomolecules has led to high sensitivity and specificity for targeted fluorescence imaging of cancer cells [63–65]. This section will introduce recent designs and developments of SPNs for *in vivo* fluorescence imaging.

3.1. Lymph node imaging

Accurate identification and characterization of lymph nodes by imaging technology is important as it can provide therapeutic and prognostic information in patients with newly diagnosed cancers [66]. Many nanoparticles have been synthesized for sentinel lymph node mapping in living mice, while their imaging performance still needs to be improved [67–70]. Particularly, advanced probes with high fluorescence brightness, long blood-circulation time and deep tissue penetration capability are desired for clinical lymph node imaging [71–74]. In a recent study of Pu's group, multilayered near-infrared (NIR) fluorescent SPNs (SPNs-M) with enhanced fluorescence brightness, deep tissue penetration, and improved biodistribution were constructed for *in vivo* fluorescence imaging applications [75]. To reveal the functionality of each layer, poly[5-octyl-1-(5-(4,4,9,9-tetrakis(4-hexylphenyl)-4,9-dihydro-s-indaceno[1,2-b:5,6-b′]dithiophen-2-yl)thiophen-2-yl)-3-(thiophen-2-yl)-4H-thieno[3,4-c]pyrrole-4,6(5H)-dione] (PDTPDTT, SP1), poly[2,6-(4,4′-bis(2-ethylhexyl) dithieno[3,2-b:2′,3′-d]silole)-alt-4,7(2,1,3-benzothiadiazole)] (PSBTBT, SP2), poly[3-(5-(9-hexyl-9-octyl-9H-fluoren-2-yl)thiophen-2-yl)-2,5-bis(2-hexyldecyl)-6-(thiophen-2-yl)-pyrrolo[3,4-c]pyrrole-1,4(2H,5H)-dione] (DPPF, SP3) and poly[2,6-(4,4-bis-(2-ethylhexyl)-4H-cyclopenta[2,1-b;3,4-b′]dithiophene)-alt-4,7(2,1,3-benzothiadizole)] (PCPDTBT, SP4) based SPNs with different nanoarchitectures were designed (Fig. 1a): SPNs with a middle silica protection layer and an outer poly(ethylene glycol) (PEG) corona (SPNs-M), bare SPNs (SPNs-B), SPNs made from nanoprecipitation with the amphiphilic triblock copolymer (F127) (SPNs-F) and SPNs with a silica shell (SPNs-Si). The silica protection layer dramatically increased the fluorescence intensities and quantum yields of SPNs, and thus SPNs-Si and SPNs-M displayed much stronger fluorescence signal than SPNs-B and SPNs-F (Fig. 1b). In addition, the outer PEG corona in SPNs-M played a respective role in improving the *in vivo* biodistribution. SPN4-M was chosen as an example for lymph node imaging in living mice because of its longest excitation and emission wavelengths as well as relatively high NIR quantum yield among the four SPNs-M. After the intradermal injection of SPN4-M into the forepaw of living mice, strong NIR fluorescence signal was clearly observed in the axillary lymph node with the signal to noise ration as high as ~85 (Fig. 1c).

3.2. Tumor imaging

The development of novel probes for early-stage diagnosis of cancer is urgently needed to increase patient survival [76]. SPNs have been developed as fluorescent probes for tumor imaging in living animals [53]. Chiu and co-workers conjugated chlorotoxin (CTX) onto the surface of PFBT (SP5) and PFDBT5 (SP6) based SPNs to endow these probes with specific targeting to the brain tumors [37]. Another previous study reported the synthesis of PFBTDBT (SP7) loaded SPN7 with surface modification of folic acid for targeted *in vivo* fluorescence imaging of hepatoma H22 tumor models [65]. Similarly, surface functionalization of folic acid led to a very high accumulation of multiblock SPNs in the xenografted KB tumors after 24 h of intravenous injection, which demonstrated their great potential for *in vivo* targeting tumor imaging [64]. Despite these progresses, applications of these previously reported SPNs for fluorescence imaging of tumors are far from ideal because their absorption and emission maximum are far away from the center wavelength (~800 nm) of the first optical window of biological tissue (between ~650 nm and 950 nm) [77]. Accordingly, a kind of NIR800 polymer with bright and narrowband emission at 800 nm was synthesized for *in vivo* tumor imaging [67]. SPN8 based on the blend of NIR800 polymer and PFDHTBT (SP8) displayed an enhanced fluorescence intensity and quantum yield due to the efficient intra-particle energy transfer. After injecting the PEGylated SPN8 into a living mouse *via* tail vein, the xenograft MCF-7 tumor was clearly observed in the fluorescence image.

3.3. Cell tracking

The *in vivo* tracking of transplanted cells is a pressing need not only for optimizing cell-based therapeutics but also for understanding many life-threatening pathological processes [78]. SPNs were recently used as a new class of labeling nanoagents for *in vivo* tracking of different cell lines [79, 80]. For example, Chan and co-workers reported the synthesis of donor-bridge-acceptor SPNs as fluorescent probes for *in vivo* tracking of cancer cells (Fig. 2a) [80]. These donor-bridge-acceptor SPNs integrated polyfluorene (PF) as donor and phthalocyanine (Pc) or boron dipyrrin (BODIPY) as acceptor. They were 3-4 times brighter and their emission bandwidths were 2.5 times narrower than the commercially available quantum dots, because the presence of the π-bridge spacer (TC6FQ) effectively increased the quantum yields of SPNs. SPN9 synthesized from PF-TC6FQ-BODIPY (SP9) was used as an example to demonstrate their applicability for biological imaging (Fig. 2b). SPN9 conjugated with streptavidin allowed for the cell-surface labeling of membrane proteins and subcellular labeling of microtubules in HeLa cells with the help of biotinylated CD326 EpCAM antibody and monoclonal anti-α-tubulin antibody, respectively. Additionally, folic acid functionalized SPN9 was readily to be applied for *in vivo* targeting and long-term monitoring of tumors. SKOV-3 ovarian carcinoma cells treated with folic acid functionalized SPN9 and bare SPN9 were subcutaneously implanted into the right and left hind flank of nude mice, respectively. The tumor in the right hind flank (red circle) clearly revealed bright NIR fluorescence, while the tumor in the left hind flank (black circle) displayed no detectable fluorescence signal (Fig. 2c). More importantly, fluorescence signal of the tumor in the right hind flank was retained at 32% even after 36 days of injection, indicating the sturdy fluorescence and excellent long-term stability of SPN9.

3.4. Drug release tracking

Tracking drug release from its vehicle is quite important to better understand the subcellular mechanisms of drug-induced therapy and therefore to rationally design new drug delivery systems [81]. In addition to cell tracking, SPNs were also applicable to track anticancer drug release by responding to pH. As reported in a previous study [82], a pH-sensitive pendant acetal modified dextran (m-dextran) was used to encapsulate doxorubicin (DOX) and NIR fluorescence poly[9,9-bis(N,N-d-imethylpropan-1-amino)-2,7-fluorene-alt-5,7-bis(thiophen-2-yl)-2,3-dimethylthi eno[3,4-b]pyrazine] (BTTPF, SP10) to fabricate SPN10. In a mildly acidic environment, the sustained release of DOX from SPN10 weakened the intra-particle fluorescence resonance energy transfer (FRET) process, resulting in corresponding fluorescence quenching of SP10 and the recovery of DOX fluorescence. *In vivo* studies well validated that SPN10 could monitor drug biodistribution, as well as indicate drug release in a non-invasive and real-time way.

3.5. Reactive oxygen specie (ROS) imaging

ROS play very important roles in homeostasis, signals transduction and stem cell differentiation [83]. Abnormal ROS levels are the hallmarks of many diseases including bacterial infection, cancer, cardiovascular disease and arthritis [22]. Thus, development of activatable probes capable of detecting ROS *in vivo* is in urgent need. By incorporating optically active dyes into SPNs, it is feasible to design smart activatable nanoprobes for imaging of diseases biomarkers, such as ROS [27, 84]. Recently, a NIR nanoprobe (SPN11) based on poly[9,9′-dihexyl-2,7-bis(1-cyanovinylene)fluorenylene*alt-co*-2,5-bis(*N*,*N*-diphenylamino)-1,4-p-henylene] (PCFDP, SP11) was designed and developed for fluorescence imaging of reactive oxygen and nitrogen species (RONS) in living mice [85]. RONS-sensitive cyanine derivatives (IR775S) were conjugated onto the surface of SPN11 through a carbodiimide-activated coupling reaction (Fig. 3a). Under excitation, SPN11 exhibited two emission peaks at 678 nm (SPN core) and 818 nm (IR775S) due to FRET. In the presence of RONS, the surface conjugated IR775S was decomposed and consequently the FRET effect within SPN11 was abolished, allowing for fluorescence imaging of RONS. Take peroxynitrite ($ONOO^-$) as an example, the emission peak of SPN11 at 678 nm increased while that at 818 nm correspondingly decreased with increasing the concentrations of $ONOO^-$ (Fig. 3b). Besides $ONOO^-$, SPN11 was also highly sensitive to hypochlorite (ClO^-) and hydroxyl radical (•OH) but not to hydrogen peroxide (H_2O_2) (Fig. 3c). Moreover, SPN11 was utilized for systemic imaging of RONS in mouse models of spontaneous *Corynebacterium bovis (C. bovis)* bacterial infection (Fig. 3d). The injected SPN11 first gradually accumulated into the infected regions within 15 min post-injection through the enhanced permeability and retention (EPR) effect, and then progressively be induced to change from unactivated (green) to activated (red) states by microenvironmental RONS, with nearly complete probe activation by 60 min (Fig. 3e).

A cocktail probe design approach based on SOs was proposed for multilocal and multicolor imaging of ClO^- in different organelles of living cells [86]. SO1 and SO2 with different π-conjugation lengths were synthesized, both of which contained phenothiazine as ClO^- sensing unit, but showed different fluorescent color responses. Nanoprecipitation of SOs and targeted amphiphilic copolymers resulted in lysosome-targeted nanoprobes (LNP) and

mitochondria-targeted nanoprobes (MNP), respectively. The mixture of LNP and MNP formed a nano-cocktail, allowing for simultaneous imaging of elevated level of ClO^- in both lysosome and mitochondria according to different fluorescence responses under selective light excitation. Although no *in vivo* data was included, this study verified the great potentials of probe cocktails for multilocal and multicolor fluorescence imaging of ClO^- in biological systems.

The detection of ClO^- in living animals was presented in another recent study by using a ratiometric strategy [87]. SP12 comprised of a ClO^--inert component, benzoxadiazole (OBT), as the energy donor and a ClO^--sensitive 4,7-bis(2-thienyl)-2,1,3-benzoselenadiazole (SeTBT) as the energy acceptor was designed and used to prepare the probe (SPN12). The SeTBT could be oxidized by ClO^- and the FRET process within SPN12 was subsequently disturbed (Fig. 4a). Thereby, the emission of SPN12 at 680 nm dramatically decreased and that at 540 nm increased, allowing for ratiometric detection (I_{540nm}/I_{680nm}) of ClO^- (Fig. 4b). SPN12 was highly sensitive to ClO^- and the limit of detection was as low as 0.5 μM. More importantly, SPN12 displayed a specific selectivity for ClO^-, as it was not responsive to other ROS or active reducing species (Fig. 4c). Therefore, SPN12 was used for ratiometric fluorescence imaging of exogenous ClO^- (Fig. 4d) and endogenous ClO^- in lipopolysaccharide (LPS)-induced peritonitis in living mice (Fig. 4e).

3.6. Glucose imaging

The continuous monitoring of blood glucose levels is very important in diabetes management [88]. Recently, SPNs were used for *in vivo* dynamic monitoring of glucose [89]. SPN13 was synthesized through nanoprecipitation of a fluorescent poly(9,9-dihexylfluorenyl-2,7-diyl) (PDHF, SP13), oxygen-sensitive phosphorescent dye (platinum(II) octaethylporphine, PtOEP) and amphiphilic functional polymer poly(styrene-co-maleic anhydride) (PSMA), following by surface conjugation with glucose oxidase (GOx). In the presence of glucose, SPN13 with enzyme conjugates behaved as a nanoreactor that depleted its internal oxygen reservoir, and the glucose concentrations were monitored by the optical signal of the oxygen transducers (Fig. 5a). Owing to the intra-particle FRET, SPN13 had a bright red phosphorescence peak at 648 nm (from PtOEP) sensitive to glucose concentration, while the weak blue fluorescence peak at 428 nm (from SP13) remained constant (Fig. 5b). The ratio of emission peak from 648 to 428 nm showed a good linear relationship with the glucose concentration in the physiologically relevant range of blood glucose (4-18 mM) (Fig. 5c). The *in vivo* response of SPN13 to blood glucose fluctuations in living mice was monitored by fluorescence imaging (Fig. 5d). The fluorescence signal increased right after the subcutaneous administration of glucose and then decreased after the injection of insulin. For the control mice without injection of glucose and insulin, the fluorescence signal remained unchanged. As many oxygen-consuming enzymes can be conjugated onto the surface of SPNs, other probes may be developed for *in vivo* imaging of a variety of small molecules such as metabolites, amino acids, neurotransmitters and drug molecules.

4. Chemiluminescence imaging

Chemiluminescence imaging is a well-established technology for various biological analysis and disease diagnosis [90–92]. The light emission of chemiluminescence is usually from chemical reactions, and therefore no external light excitation is needed [93, 94]. Compared with traditional photon emission based detection methods, chemiluminescence imaging exhibits many prominent advantages including obviously reduced background signal interference and fairly low photodamage [95].

4.1. ROS and RNS multiplex imaging

For the rapid and real-time multiplex imaging of drug-induced ROS and RNS in living animals, poly(2,7-(9,9-dioctylfluorene)-alt-4,7-bis(thiophen-2-yl)benzo-2,1,3-thiadiazole) (PFODBT, SP14) was transformed into a sensing probe with the incorporation of H_2O_2 reactive chemiluminescent substrate, bis-(2,4,5-trichloro-6-(pentyloxycarbonyl)phenyl)oxalate (CPPO) and $ONOO^-$ responsive NIR dye (IR775S) [96]. The designed SPN14 could be applied for fluorescence imaging of $ONOO^-$ and chemiluminescence imaging of H_2O_2 (Fig. 6a). In the presence of $ONOO^-$, IR775S was irreversibly degraded and the FRET from SP14 to IR775S was consequently abolished, resulting in an emission enhancement at 680 nm for SP14 and emission decrease at 820 nm for IR775S (Fig. 6b). In the presence of H_2O_2, luminescence without external light excitation was generated through the chemiluminescence resonance energy transfer (CRET) from the photons generated the chemical reaction between CPPO and H_2O_2 within the nanoparticles (Fig. 6c). With increasing the concentration of $ONOO^-$ and H_2O_2, both *in vitro* fluorescence and chemiluminescence signals correspondingly varied. These signal responses allowed for real-time multiplex imaging of ROS and RNS in the living mice suffered from drug-induced hepatotoxicity (Fig. 6d). Both chemiluminescence and ratiometric fluorescence signals increased in the mice that received overdosed drugs such as analgesic and anti-pyretic acetaminophen (APAP) or anti-tuberculosis agent isoniazid (INH) followed by the intravenous injection of SPN14. This proved that SPN14 can be used for *in vivo* monitoring of drug-induced hepatic oxidative and nitrosative stress.

4.2. H_2O_2 imaging

To improve the imaging performance, SPNs with amplified chemiluminescence were developed according to the mechanism of chemically initiated electron exchange luminescence (CIEEL) [97]. As demonstrated in Fig. 7a, the oxidation reaction between H_2O_2 and peroxalate bis(2,4,6-trichlorophenyl) oxalate (TCPO) produced a high energy intermediate (1,2-dioxetanedione). Through obtaining an electron from the SPs, the intermediate underwent a reduction reaction and gave rise to the SP radical cation and carbon dioxide radical anion. Then, the back electron transfer occurred between the cation and anion to produce excited SPs, ultimately leading to luminescence signals. Accordingly, the key step of the CIEEL that determined the chemiluminescence efficiency of SPNs was the intermolecular electron transfer from SPs to the high energy intermediate. Therefore, five polyfluorene derivatives with different molecular orbitals were aligned with the high energy intermediate to facilitate the efficient electron transfer. At the same mass concentration of SPs, poly[(9,9′-dioctyl-2,7-divinylene-fluorenylene)-alt-2-methoxy-5-(2-

ethylhexyloxy)-1,4-phenylene] (PFPV, SP15) based SPN15 displayed the highest chemiluminescence quantum yield (2.30×10^{-2} einsteins/mol) because the intermolecular electron transfer between SP15 and the 1,2-dioxetanedione was the most facilitated. Thus, SPN15 efficiently detected H_2O_2 *in vitro* with the limit of detection as low as 5 nM. After doping with silicon 2,3-naphthalocyanine bis(trihexylsilyloxide) (NIR775), SPN15 had a red-shifted chemiluminescence wavelength with the maximum at 775 nm and thus could be applied for *in vivo* imaging of LPS-induced neuroinflammation in mouse models (Fig. 7b and c). After the intracerebral administration of SPN15, the chemiluminescence intensity for the LPS-treated mice was ~1.7 times higher than that for the control mice, which was reduced by 21% upon glutathione (GSH) remediation. This underlying mechanism can also be used to improve the chemiluminescence efficiency of other CRET systems.

Recently, Seo and co-workers proposed another rational nanophotonic way to increase chemiluminescence signal of SPN probes with an emission maximum at 700 nm through bridging the energy gaps between peroxalates and emitters using an energy relay dye [98]. Upon addition of H_2O_2, the doped 'relay molecule' (BODIPY dye) in SPNs effectively accepted the energy from the chemically excited intermediate of peroxalates (CPPO) and transferred it to the polymer aggregates (DPA-CN-PPV, SP16) within the nanoparticles by consecutive intra-particle energy transfer. With the NIR emission at 700 nm, the BODIPY-doped SPN16 not only showed a fairly high tissue penetration depth (> 12 mm), but also presented a low limit of detection toward H_2O_2 down to 1 nM. These combined merits of this probe enabled sensitive *in vivo* chemiluminescence imaging of inflammation in LPS-induced arthritis and peritonitis models.

4.3. Superoxide anion imaging

The sensitive and specific detection of superoxide anions ($O_2^{\bullet-}$) remains to be challenging because of its very low concentration in biological systems [99, 100]. Therefore, it is highly desirable to develop ultrasensitive probes for *in vivo* imaging of $O_2^{\bullet-}$ [101]. In a recent study, SP17 comprised imidazopyrazinone as the $O_2^{\bullet-}$ specific CRET donor and the PFBT (SP5) as the CRET acceptor was used to fabricate SPN17 for $O_2^{\bullet-}$ imaging (Fig. 8a). Through an energy transfer process, the photon produced by specific reaction between imidazopyrazinone and $O_2^{\bullet-}$ was transferred to PFBT, leading to the generation of luminescence signal. The luminescence signal increased linearly with the concentrations of $O_2^{\bullet-}$ and the limit of detection was estimated to be as low as 19.3 pM. The ultra-high sensitivity of SPN17 toward $O_2^{\bullet-}$ enabled chemiluminescence imaging of $O_2^{\bullet-}$ in both LPS-induced inflammation models and tumor models. The intratumorally injected SPN17 displayed much stronger chemiluminescence in tumor tissue than that in normal tissue (Fig. 8b). The signal intensity in tumor tissue was 3.0-times higher than that in normal tissue (Fig. 8c). Treatment of Tiron (a typical superoxide scavenger) could reduce the chemiluminescence signal in tumor tissue, indicating the decreased level of $O_2^{\bullet-}$. While SPN17 was claimed to be as the most sensitive probe for $O_2^{\bullet-}$ detection by far, the visible emission wavelength (560 nm) made it not suitable for *in vivo* imaging of $O_2^{\bullet-}$.

5. Photoacoustic (PA) imaging

PA imaging, a new non-ionizing imaging mode that integrates optical excitation with ultrasonic detection based on the PA effect, has gained extensive attention [102–105]. PA imaging can provide deeper tissue imaging penetration and higher spatial resolution as compared with traditional optical imaging techniques due to its minimized light scattering issue [106–109]. In general, the utilization of PA contrast agents is often required as most biomolecules do not generate efficient PA signals when excited at the NIR wavelength [22]. A number of nanoparticles including inorganic metallic nanoparticles, up-conversion nanoparticles, carbon nanotubes and porphysomes have been used as contrast agents for PA imaging applications [12, 110–114]. However, these nanoparticles have their own limitations, and there are strong interests in developing more efficient PA imaging agents [115, 116]. Recently, SPNs have been exploited as an alternative class of PA imaging agents [117–122].

5.1. Lymph node imaging

SP4 with a strong absorption in the NIR region was transformed into SPN4 for *in vivo* PA imaging applications [123]. The resulted SPN4 generated higher PA signals than two of the best current contrast agents, single-walled carbon nanotubes (SWNTs) and gold nanorods (GNRs), on a per mass basis. Moreover, after continuous laser exposure, the PA signal of GNRs decreased significantly, while no PA signal attenuation was observed for SPN4 under the same conditions. The excellent PA property and superior photostability of SPN4 enabled it to be used as a contrast agent for whole-body lymph node PA mapping in living mice at a low systemic injection mass (50 μg). After intravenous administration of SPN4, obvious PA signal augmentation was detected in the lymph nodes. The utilization of SPNs for PA imaging of lymph nodes was also reported by Liu and co-workers [41]. In this study, SON3 probe based on SO3 had many merits, such as strong NIR absorption, good cytocompatibility, excellent PA contrast and quick body clearance. The PA signal of sentinel lymph node was clearly visualized after the injection of SON3 for 10 min. The signal intensity started to slowly decrease at 20 min but still persisted at 90 min post-injection.

5.2. Vascular imaging

Intravital vascular imaging has the potential to be a powerful tool for minimally invasive diagnosis and visualization of some diseases [124–126]. However, the blood is an endogenous strong light absorber in biological tissues that can generate strong PA signal, which will interfere the vascular PA imaging performance [127]. Consequently, design and development of PA probes with higher PA signal than surrounding vasculature is highly desirable. To satisfy this requirement, a PIID-DTBT (SP18) based novel nanoprobe (SPN18) with broad and strong optical absorption in the visible-light region was developed [127]. SPN18 had better PA performance than the blood, and therefore the signal could be accurately extracted from the background of vascular-rich tissues. In another study [128], a nanoprobe for PA imaging of brain vasculature was designed and synthesized based on poly[9,9-bis(4-(2-ethylhexyl)phenyl)fluorene-alt-co-6,7-bis(4-(hexyloxy)phenyl)-4,9-di(thiophen-2-yl)-thiadiazoloquinoxaline] (PFTTQ, SP19). SPN19 showed a strong absorption in the NIR range with a very high non-radiative quantum yield of almost 100%

owing to the electron-deficiency of thiadiazoloquinoxaline derivatives. Thus, SPN19 was applied for brain vasculature imaging with enhanced PA contrast. The PA intensity of blood vessels was improved by ~3-fold after the retroorbital injection of SPN19 as compared to the intrinsic signal. In a recent study, our group synthesized a SP20 based PA contrast agent with broadband absorption property in both NIR-I and NIR-II windows for brain vasculature imaging [129]. The formed SPN20 could clearly visualize the brain vasculature of living rats in NIR-II window PA imaging, which showed 1.5-times higher signal-to-noise ratio (SNR) as compared with NIR-I PA window imaging.

5.3. Tumor imaging

To improve PA imaging of tumor, a series of SPNs composed of low-bandgap diketopyrrolopyrrole (DPP)-based SPs were synthesized and their PA properties were systematically studied and compared [121]. Among these SPNs, SPN21 fabricated form SP21 had the brightest PA signal because of the strongest electron donor-acceptor backbone structure and narrowest band gap. This great advantage allowed SPN12 to be used as an excellent nanoprobe for *in vivo* tumor imaging with 5.3-fold PA signal enhancement after systemic administration (30 μg/mouse). This random screening approach adopted in this study was quite time-consuming and required great efforts. Exploration of novel, facile and rational technologies to prepare probes with amplified PA brightness still remains a great challenge.

A rational strategy for PA amplification is incorporating of electron-deficient structure units into polymer backbone as they can promote the non-radiative decay and in turn quench the fluorescence for enhanced heat generation [130]. As reported in a recent study of our group, SPN22 based on the synthesized SP (SP22) with 10% doping of benzothiadiazole (BT) as an electron-deficient structure unit displayed a 1.7-fold PA amplification compared with the corresponding SPNs. After the surface conjugation with cyclic-RGD, SPN22 was highly promising to effectively delineate the xenografted 4T1 tumors in living mice. The PA intensity in tumor tissues increased by 4.7-fold after the systemic administration of targeted SPN22.

Surface coating of SPNs with silica layer was reported to be another strategy to amplify their PA brightness [131]. Poly(cyclopentadithiophene-alt-diketopyrrolopyrrole) (PDPPCPDT, SP23) and PCPDTBT (SP4) were recently developed into silica-coated SPNs (SPN23-SiO_2 and SPN4-SiO_2) through nanoprecipitation and surface engineering (Fig. 9a). At the same mass concentration, both SPN23-SiO_2 and SPN4-SiO_2 displayed much brighter PA signal as compared to SPN23 and SPN4. The PA amplitudes of silica-coated SPNs were ~1.4 higher than that of the corresponding uncoated SPNs for both SPN23 and SPN4 (Fig. 9b). This amplified PA property may be due to the higher heat interfacial conductance for the interface between the silica layer and water as compared with that between the SP core and water (Fig. 9c). Considering the enhanced PA property, SPN23-SiO_2 was used for *in vivo* targeted PA imaging of xenografted tumors after the surface conjugation with PEG and cyclic-RGD. PA signal in tumor regions gradually increased over time and reached maximum at 8 h post-injection *via* tail vein for both SPNs. While the SPN23-SiO_2-RGD group had much higher

PA intensities in tumor regions as compared to those for SPN23-SiO_2-PEG at each post-injection time point because of higher accumulation of SPNs (Fig. 9d).

One issue should be noted is that the SPNs prepared *via* miniemulsion or nanoprecipitation potentially encounter dissociation and aggregation during blood circulation, thus leading to changed optical property and poor biodistribution [132]. To avoid this issue, structurally stable amphiphilic SPs and SOs capable of spontaneously self-assembling into homogenous SPNs were reported for *in vivo* tumor imaging [133, 134]. For example, SON4 self-assembled from amphiphilic SO4 attached with hydrophilic PEG side chains not only had a higher structural stability, but also displayed much brighter PA signal compared to their counterparts synthesized by nanoprecipitation [134]. These properties along with the PEG-passivated surface allowed SON4 probe to efficiently accumulate into tumors of living mice, permitting PA imaging of tumors with high signal-to-background ratios. In another study, the influence of surface PEG grafting density on optical property and imaging performance of SPNs was determined to ensure the design of self-assembled nanoprobes better performance [135]. The PEG density had no significant impact on PA property, but high PEG grafting density was beneficial for the enhanced fluorescence brightness of SPNs. By virtue of the abundant surface PEG, the developed SPNs showed a great potential for *in vivo* PA and fluorescence dual mode imaging of tumors.

5.4. ROS imaging

In vivo PA imaging of ROS was realized by doping SPN4 with a ROS-sensitive cyanine dye derivative (IR775S) [123]. The PA spectrum of the resulted probe (RSPN4) showed three peaks at 700, 735 and 820 nm. In the presence of ROS, the PA peak at 735 nm decreased obviously and that at 820 nm almost disappeared due to the oxidative decomposition of IR775S by ROS, while the peak at 700 nm remained unchanged (Fig. 10a and b). This led to the ratiometric PA signal (PA_{700}/PA_{820}) and allowed for accurate detection of certain ROS including $ONOO^-$ and ClO^-. The feasibility to use RSPN4 as an activatable probe for *in vivo* imaging of ROS was demonstrated on the zymosan-induced mice models of acute oedema. The PA signal of RSPN4 at 820 nm significantly decreased and that at 700 nm did not have obvious changes for the zymosan treated mice (Fig. 10c). In contrast, the PA signal at both 820 and 700 nm remained unchanged for the saline treated mice. Moreover, the ratiometric PA signal (PA_{700}/PA_{820}) gradually increased after the treatment of zymosan, suggesting the activation of RSPN4 by the generated ROS (Fig. 10d).

Selective ratiometric PA imaging of $ONOO^-$ was achieved using organic semiconducting nanoprobes [136]. The probe (SON5) was synthesized *via* nanoprecipitation of ROS-active NIR dye, boronate-caged boron-dipyrromethene (BBD, SO5) and $ONOO^-$ responsive bulky boranes (such as triphenylborane) with the assistance of an amphiphilic triblock copolymer. The presence of excess bulky boranes effectively inhibited the reaction between BBD and oxidative species other than $ONOO^-$ owing to their stronger oxidative capability. Upon addition of ROS, the PA signal at 750 nm significantly increased while that at 680 nm remained nearly unchanged, allowing for ratiometric signal response (PA_{750}/PA_{680}) toward $ONOO^-$ with high specificity (Fig. 11a and b). The ratiometric PA signal linearly increased as the concentrations of $ONOO^-$ with a limit of detection about 10^{-7} M, suggesting SON5

probe was ideal to detect $ONOO^-$ at pathologically relevant concentrations (Fig. 11c). Considering the high selectivity and relatively fast kinetics, SON5 was used for *in vivo* PA imaging of $ONOO^-$ on the subcutaneous 4T1 xenograft tumors of living mice with or without pre-treatment of an ROS scavenger, *N*-acetyl-l-cysteine (NAC) (Fig. 11d). The PA signal at 750 nm increased obviously after the injection of SON5, and the NAC treatment reduced the signal. The *in vivo* ratiometric PA signal ($\Delta PA_{750}/\Delta PA_{680}$) gradually increased and reached its maximum at 4 h post-injection for untreated mice (Fig. 11e), suggesting the effective activation of SON5 towards $ONOO^-$. While, the $\Delta PA_{750}/\Delta PA_{680}$ in the NAC-treated mice slightly increased over 24 h because of the scavenging of ROS.

Recently, an activatable and degradable PA probe for *in vivo* imaging of ClO^- was developed through a self-assembly approach [137]. A NIR absorbing SO6-PEG with a **π**-conjugated but ClO^- oxidizable backbone integration was used to encapsulate NIR775 and self-assembled into SON6. The oligomer could be degraded by ClO^-, while the encapsulated NIR775 remained intact. As a consequence, the PA intensity of SON6 at 680 nm gradually decreased, but the peak at 780 nm remained nearly unchanged with the addition of ClO^-. Thus, SON6 displayed high sensitive and specific ratiometric PA signal (PA_{780}/PA_{680}) toward ClO^-, allowing for ratiometric PA imaging of ClO^- in the xenografted tumors of living mice.

5.5. pH imaging

Detection of pH in biological systems is crucial as it is a critical physiological parameter related to cellular and tissue homeostasis, and aberrant pH is usually associated with many diseases [138–141]. Our group developed an activatable PA nanoprobe based on F-DTS (SO7) for ratiometric *in vivo* imaging of pH [142]. The SON7 was synthesized with SO7 as the inert PA matrix and a boron-dipyrromethene dye (pH-BDP) as the PA enhancer and pH indicator. The photo-induced electron transfer occurred between SO7 and pH-BDP, resulting in quenched fluorescence and in turn amplified PA signal. The PA intensity of SON7 at 750 nm decreased significantly as the decrease of pH, while the intensity at 680 nm barely changed (Fig. 12a). $SON7_{50}$ with 50 w/w% doping amount of pH-BDP could be used for pH quantification with a good linearity between ratiometric PA signal (PA_{680}/PA_{750}) and pH in the range of 7.4 to 5.5 (Fig. 12b). *In vivo* PA imaging of pH using $SON7_{50}$ was performed on the HeLa xenograft tumor models (Fig. 12c). After the intravenous administration of $SON7_{50}$, the PA intensity increment at 680 nm (ΔPA_{680}) substantially increased over time and reached its plateau at 3 h post-injection, while the PA intensity increment at 750 nm (ΔPA_{750}) slightly increased (Fig. 12d). The *in vivo* ratiometric PA signal ($\Delta PA_{680}/\Delta PA_{750}$) thus increased over time and the pH in the tumor could be roughly estimated to be ~6.3 (Fig. 12e).

5.6. Protein sulfenic acid imaging

Oxidative modification of cysteine in proteins to sulfenic acids (SOH) is an important post-translational modification and plays a pivotal role in regulating protein functions and oxidative signal transduction [143]. Protein sulfenic acids are closely related to many pathological conditions such as neurodegenerative diseases, cancer, cardiac dysfunction, and reperfusion injury, while their detections in living systems have been rarely reported [144–

146]. Our group reported a reaction-based SP nanoprobes (rSPNs) with NIR absorption for *in vivo* PA imaging of protein sulfenic acids [147]. The 1,3-cyclohexanedione groups on the surface of nanoprobes enabled their specific reaction and covalent binding to SOH sites of oxidized proteins (Fig. 13a). PCPDTBT (SP4) based rSPN4 with strong absorption in the NIR region was used as a probe for *in vivo* PA imaging. The PA brightness at 680 nm was almost the same for rSPN4 with and without bovine serum albumin (BSA) or BSA-SOH, suggesting the reactions with protein sulfenic acids did not affect the PA property of rSPN4 (Fig. 13b). The feasibility to use rSPN4 as a probe for *in vivo* protein sulfenic acids detection was investigated on the xenograft HeLa tumor mouse model with the nonreactive SPN4 as a control. The injection of nanoprobes increased tumor PA intensities for both groups over time (Fig. 13c). At 36 h of post-injection, tumor PA intensity in the rSPN4-injected mice was 1.3-fold higher than that in the SPN4-injected mice (Fig. 13d). The real-time *in vivo* spectra of tumors showed that the PA signal at 680 nm for rSPN4 was 1.5-fold higher than that for SPN4 (Fig. 13e). The higher PA signal was attributed to the enhanced accumulation of rSPN4 caused by their covalent bonding with protein sulfenic acids in the oxidative microenvironment of tumors. This study indicated that rSPN4 was promising for imaging of protein sulfenic acids in vivo.

5.7. Thrombus imaging

Acute venous thrombosis is a potentially fatal menace and accurate diagnosis of early thrombus allows timely treatment intervention to prevent embolus from formation [148]. Fan and co-workers recently developed a cyclic RGD functionalized SON (cRGD-SON8) based on perylene-3,4,9,10-tetracarboxylic diimide (PDI, SO8) for selectively PA imaging of early thrombus in living mice [149]. The cRGD-SON8 displayed excellent PA property, good optical and colloidal stability, and long blood-circulating half-life (how long), allowing for PA imaging of $FeCl_3$-induced mouse model of jugular vein thrombus (Fig. 14a). After the tail vein injection of cRGD-SON8, PA intensity in the early thrombus group obviously increased, which was 4-fold greater than that in the control, blocking and old thrombus groups (Fig. 14b and c). The cRGD-SON8 could distinguish early thrombus from old ones because its surface functionalized cRGD had a high binding affinity to Glycoprotein IIb/IIIa that is expressed abundantly in early thrombus. Meanwhile, it was also practicable to timely monitor the obstructive degree and therapeutic efficiency of thrombus in blood vessels by using cRGD-SON8 as probe.

6. Phototherapy of cancer

In addition to the early-stage diagnosis, nanomaterials have shown great potential in the treatments of cancers, in particular through photo-induced damages [150–155]. Currently, various inorganic nanoparticles have been applied for cancer phototherapy, while these inorganic nanomaterials are nonbiodegradable and have the potential issue of toxicity [156–158]. In contrast, SPNs have attracted more and more research interests in phototherapy as a result of their excellent optical property [159]. In this section, recent design and progress of SPNs used for photothermal and photodynamic therapy of cancer are discussed.

6.1. Photothermal therapy

Various SPs, such as polyaniline, polypyrrole (PPy) and poly(3,4-ethylenedioxythiophene)/poly(4-styrenesulfonate) have been transformed into SPNs for photothermal therapy [160–162]. However, the efficacies of these reported SPNs were constrained because of their weak and broad absorption band in the NIR region. To improve the photothermal conversion efficiency of SPNs, many attempts have been made to synthesize SPs as novel photothermal agents with stronger and sharper NIR absorbance peaks [159, 163, 164]. For example, a donor-acceptor structured porphyrin-containing SP (PorCP, SP24) with the absorption maximum at 799 nm was synthesized for photothermal cancer therapy [165]. The formed SPN24 exhibited a high photothermal conversion efficiency of 63.8%, which was relatively high as compared with that of commonly used photothermal agents.

For optimized cancer therapy, it is imperative to develop a theranostic nanoplatform that integrates both diagnostic element and therapeutic agent [44, 166–168]. By virtue of the real-time imaging, theranostic agents can identify the location of tumor, detect the accumulation of agents, and monitor the therapeutic efficiency. The result is the ablation of tumors with higher specificity and sensitivity [169–171]. For example, a biocompatible electron donor-acceptor conjugated SPN with light-harvesting unit was used for highly effective PA imaging guided photothermal therapy of cancers [172]. In another study, SON8 with [^{64}Cu]-labeling was developed into a multifunctional theranostic agent for positron emission tomography (PET) and PA imaging guided photothermal therapy of cancers [173].

We recently reported an intra-particle molecular orbital engineering approach to simultaneously enhance PA brightness and photothermal therapy efficacy of SPNs for *in vivo* imaging and treatment of cancers [116]. The theranostic SPN4 was prepared *via* nanoprecipitation of PCPDTBT (SP4) and (6,6)-phenyl-C71-butyric acid methyl ester (PC70BM) as electron donor and acceptor, respectively. The energy level alignment favored the photo-induced electron transfer within SPN4, resulting in quenched fluorescence and enhanced nonradiative heat generation under laser irradiation (Fig. 15a). With increasing the doping amount of PC70BM, the fluorescence intensity of SPN4 was gradually quenched (Fig. 15b), while the PA intensity obviously increased (Fig. 15c). Moreover, PC70BM doping also contributed to the enhanced photothermal therapy efficiency of SPNs, as much higher temperature was observed under laser irradiation (Fig. 15d). Because of the best PA and photothermal performance, SPN4 with 20 w/w% doping amount of PC70BM (SPN4-F20) was chosen for *in vivo* applications with SPN4-F0 as a control. The PA signal in tumors reached its maximum after the administration of SPNs for 6 h, and the intensity for SPN-F20 injected mice was 1.8-fold of that for SPN-F0 treated mice. Under laser irradiation, the tumor temperature of SPN4-F20 injected mice was 1.3- and 1.7-fold of that for SPN4-F0 and saline injected mice at all the time points, respectively (Fig. 15e and f). Tumor growth in SPN4-F20 injected mice was successfully inhibited for 16 days, suggesting the potential capability of SPN4-F20 for therapeutic applications (Fig. 15g).

6.2. Photodynamic therapy

In general, SPs can directly sensitize oxygen molecules to produce ROS upon light excitation [174]. However, their applications for photodynamic therapy of cancers are rarely

reported, which may be mainly because of the low ROS generation yield and limited tissue penetration ability of general SPs. In the recent studies from Wu's group, photosensitizers were loaded into or conjugated to SPNs for photodynamic therapy of cancers [175–177]. In these systems, SPs could efficiently absorb and transfer the excitation energy to photosensitizer units, leading to the amplified generation of singlet oxygen under excitations. In another study, a two-photon-excited SPN25 based on polythiophene quaternary ammonium salt (SP25) was proposed as a smart therapeutic agent for amplified photodynamic cancer therapy benefited from its deep tissue penetration capability and strong two-photon-induced singlet oxygen generation [178].

A novel strategy called enzyme-enhanced phototherapy (EEPT) was developed for the enhanced photodynamic cancer therapy [179]. SP5 with light-harvesting property and SP6 with deep-red emission were used to prepare SPN5-6 *via* nanoprecipitation. The SPN5-6 was further covalently conjugated with GOx to form SPN5-6-GOx (Fig. 16a). In the presence of SPN5-6-GOx, the glycometabolism can produce abundant H_2O_2 as the glucose content is very high in malignant tumors. Under light irradiation, the generated H_2O_2 was split into hydroxyl radicals to kill cancer cells effectively. The generated hydroxyl radicals by photolysis of H_2O_2 was detected by terephthalic acid (TA), as its oxidation by hydroxyl radicals produced fluorescent 2-hydroxyterephthalic acid (TAOH), as shown in Fig. 16b. The fluorescence intensity increased as prolonging the irradiation time, suggesting more and more hydroxyl radicals were generated (Fig. 16c). While, no obvious hydroxyl radical generation in the absence of SPN5-6-GOx or light, as no fluorescence intensity was detected (Fig. 16d). Moreover, SPN5-6-GOx displayed a long-term retention effect in tumor sites, which was confirmed by *in vivo* fluorescence imaging. Therefore, SPN5-6-GOx was used for photodynamic therapy of tumors in living mice. The volume of tumors obviously reduced after the EEPT treatment as compared with the other treatments (Fig. 16e and f).

Despite the therapeutic efficiencies of photodynamic therapy, complete tumor ablation through photodynamic therapy has rarely been successful. This should be partially attributed to the short lifetime (< 3 μs) and small radius of action (< 0.3 μm) of singlet oxygen species as well as hypoxia microenvironment of tumor [180–182]. Therefore, combining photodynamic therapy with chemotherapy or photothermal therapy is thought to further improve therapeutic efficacy [183–185]. For instance, two SPs, poly[9,9-bis(2-(2-(2-methoxyethoxy)ethoxy)-ethyl)fluorenyldivinylene]-alt-4,7-(2,1,3-be-nzothiadiazole) (PFVBT, SP26) with efficient ROS production capability, and poly[(4,4,9,9-tetrakis(4-(octyloxy)phenyl)-4,9-dihydro-s-indacenol-dithiophene-2,7-diyl)-alt-co-4,9-bis(thiophen-2-yl)-6,7-bis(4-(hexyloxy)phenyl)-thiadiazolo-quinoxaline] (PIDTTTQ, SP27) with strong NIR absorption and excellent photothermal conversion ability were co-loaded into SPNs [186]. The co-loaded SPNs displayed a high singlet oxygen quantum yield of 60.4% and an impressive light-to-heat conversion efficiency of 47.6%. By conjugating with anti-HER2 affibody, the resultant anti-HER2-SPNs were applied for targeted photodynamic and photothermal therapy of HER2 overexpressing tumors with ~53% of tumor suppression efficiency.

In another study, a donor-acceptor-donor structured molecule, 3,6-bis(5-(4-(diphenylamino)-phenyl)thiophen-2-yl)-2,5-bis(2-ethylheptyl)pyrrolo[3,4-c]pyrrole-1,4(2H,5H)-dione (DPP-

TPA, SO9) was used to synthesize SON9 for PA imaging guided photodynamic and photothermal synergistic therapy [187]. Triphenylamine (TPA), as a typical donor was conjugated to the diketopyrrolopyrrole core for bathochromic shift absorption and charge transport capacity enhancement. In the absorption spectrum, SON9 displayed an obvious bathochromic-shift with the maximum absorption peak at 660 nm (Fig. 17a). For phototherapy applications, SON9 could induce obvious singlet oxygen generation and temperature increase under 660 nm laser irradiation (Fig. 17b and c). Efficient cellular uptake of SON9 into cancer cells allowed for the intracellular ROS generation and cell ablation under laser irradiation (Fig. 17d–f). Under the guidance of PA imaging, SON9 showed a tumor ablation capability through photodynamic/photothermal synergetic therapy (Fig. 17g).

7. Conclusion and outlooks

This review describes the recent progress on SPNs for *in vivo* molecular imaging and cancer phototherapy. The intrinsic advantages of SPNs including excellent optical properties and good photostability enable them to act as desired and versatile optical nanoagents for fluorescence, chemiluminescence and PA imaging. It is also feasible to use SPNs as phototherapeutic agents for cancer phototherapy including photothermal and photodynamic therapy. Surface conjugation of targeting ligands increases the accumulation of SPNs into tumor sites, making the diagnosis and therapy more accurate and effective. Inorganic nanoparticles or drugs may also be loaded into SPNs to generate multifunctional theranostic nanoplatforms for multi-modal imaging guided phototherapy and chemotherapy of different diseases.

Applications of SPNs for *in vivo* molecular imaging and phototherapy have achieved significant progress, but there are still some important issues that need to be addressed. SPNs have been reported to show minimal cytotoxicity, and a pilot toxicological study in balb/c mice has shown good *in vivo* biocompatibility [46]. However, comprehensive investigations of absorption, distribution, metabolism and excretion of SPNs in living bodies have not reported yet. Careful design to reduce the dimension of SPNs below 5 nm is important as nanoparticles with such a small size have fast clearance from human bodies via urinary excretion. Oral or local administration rather than intravenous injection in some specific diseases settings is another strategy to reduce the accumulation and retention of SPNs in the body. Potential influences of SPNs on the fate and functions of some cell types, such as stem cells, red blood cells and immune cells are largely unknown and need to be studied. More effective strategies to improve the diagnostic and therapeutic performance as well as to reduce the dosage of administration should be further explored through new chemistry, nanoscience and biology.

The emergence of SPNs in nanomedicine and molecular imaging promises new opportunities to better understand, detect and treat various life-threatening diseases. Integration of molecular biology into the design of SPNs should be an effective way to further advance their adventure in life science and push them into pre-clinical and even clinical applications. With the rapid progress of nanotechnology, SPN can serve as a versatile nanoplatform for emerging biomedical applications.

Acknowledgments

K.P. thanks Nanyang Technological University (Start-Up grant: NTU-SUG: M4081627.120) and Singapore Ministry of Education (Academic Research Fund Tier 1: RG133/15 M4011559 and Academic Research Fund Tier 2 MOE2016-T2-1-098) for the financial support. J. R. thanks the financial support of NIH grans (R01 DK099800 and U54CA151459).

References

1. Wang Y-J, Larsson M, Huang W-T, Chiou S-H, Nicholls SJ, Chao J-I, et al. The use of polymer-based nanoparticles and nanostructured materials in treatment and diagnosis of cardiovascular diseases: Recent advances and emerging designs. Prog Polym Sci. 2016; 57:153–78.
2. Kamaly N, Xiao Z, Valencia PM, Radovic-Moreno AF, Farokhzad OC. Targeted polymeric therapeutic nanoparticles: design, development and clinical translation. Chem Soc Rev. 2012; 41:2971–3010. [PubMed: 22388185]
3. Melancon MP, Zhou M, Li C. Cancer theranostics with near-infrared light-activatable multimodal nanoparticles. Acc Chem Res. 2011; 44:947–56. [PubMed: 21848277]
4. Howes PD, Chandrawati R, Stevens MM. Colloidal nanoparticles as advanced biological sensors. Science. 2014; 346:1247390. [PubMed: 25278614]
5. McCarthy JR, Weissleder R. Multifunctional magnetic nanoparticles for targeted imaging and therapy. Adv Drug Delivery Rev. 2008; 60:1241–51.
6. Mura S, Nicolas J, Couvreur P. Stimuli-responsive nanocarriers for drug delivery. Nat Mater. 2013; 12:991–1003. [PubMed: 24150417]
7. Blanco E, Shen H, Ferrari M. Principles of nanoparticle design for overcoming biological barriers to drug delivery. Nat Biotechnol. 2015; 33:941–51. [PubMed: 26348965]
8. Dahlman JE, Barnes C, Khan OF, Thiriot A, Jhunjunwala S, Shaw TE, et al. In vivo endothelial siRNA delivery using polymeric nanoparticles with low molecular weight. Nat Nanotechnol. 2014; 9:648–55. [PubMed: 24813696]
9. Xu R, Zhang G, Mai J, Deng X, Segura-Ibarra V, Wu S, et al. An injectable nanoparticle generator enhances delivery of cancer therapeutics. Nat Biotechnol. 2016; 34:414–8. [PubMed: 26974511]
10. Chinen AB, Guan CM, Ferrer JR, Barnaby SN, Merkel TJ, Mirkin CA. Nanoparticle probes for the detection of cancer biomarkers, cells, and tissues by fluorescence. Chem Rev. 2015; 115:10530–74. [PubMed: 26313138]
11. Huynh E, Leung BY, Helfield BL, Shakiba M, Gandier J-A, Jin CS, et al. In situ conversion of porphyrin microbubbles to nanoparticles for multimodality imaging. Nat Nanotechnol. 2015; 10:325–32. [PubMed: 25822929]
12. Rieffel J, Chen F, Kim J, Chen G, Shao W, Shao S, et al. Hexamodal imaging with porphyrin-phospholipid-coated upconversion nanoparticles. Adv Mater. 2015; 27:1785–90. [PubMed: 25640213]
13. Liu J, Liu Y, Bu W, Bu J, Sun Y, Du J, et al. Ultrasensitive nanosensors based on upconversion nanoparticles for selective hypoxia imaging in vivo upon near-infrared excitation. J Am Chem Soc. 2014; 136:9701–9. [PubMed: 24956326]
14. Qian X, Gu Z, Chen Y. Two-dimensional black phosphorous nanosheets for theranostic nanomedicine. Mater Horiz. 2017; 4:800–16.
15. Smith BR, Ghosn EEB, Rallapalli H, Prescher JA, Larson T, Herzenberg LA, et al. Selective uptake of single-walled carbon nanotubes by circulating monocytes for enhanced tumour delivery. Nat Nanotechnol. 2014; 9:481–7. [PubMed: 24727688]
16. Jiang W, Kim BY, Rutka JT, Chan WC. Nanoparticle-mediated cellular response is size-dependent. Nat Nanotechnol. 2008; 3:145–50. [PubMed: 18654486]
17. Thanh NT, Green LA. Functionalisation of nanoparticles for biomedical applications. Nano Today. 2010; 5:213–30.
18. Elsabahy M, Wooley KL. Design of polymeric nanoparticles for biomedical delivery applications. Chem Soc Rev. 2012; 41:2545–61. [PubMed: 22334259]

19. Wu C, Schneider T, Zeigler M, Yu J, Schiro PG, Burnham DR, et al. Bioconjugation of ultrabright semiconducting polymer dots for specific cellular targeting. J Am Chem Soc. 2010; 132:15410–7. [PubMed: 20929226]
20. Wu C, Chiu DT. Highly fluorescent semiconducting polymer dots for biology and medicine. Angew Chem, Int Ed. 2013; 52:3086–109.
21. Ye F, Wu C, Jin Y, Chan Y-H, Zhang X, Chiu DT. Ratiometric temperature sensing with semiconducting polymer dots. J Am Chem Soc. 2011; 133:8146–9. [PubMed: 21548583]
22. Lyu Y, Pu K. Recent advances of activatable molecular probes based on semiconducting polymer nanoparticles in sensing and imaging. Adv Sci. 2017; 4:1600481.
23. Cui Q, Wang X, Yang Y, Li S, Li L, Wang S. Binding-directed energy transfer of conjugated polymer materials for dual-color imaging of cell membrane. Chem Mater. 2016; 28:4661–9.
24. Gong X, Ma W, Ostrowski JC, Bazan GC, Moses D, Heeger AJ. White electrophosphorescence from semiconducting polymer blends. Adv Mater. 2004; 16:615–9.
25. Heeger AJ. Semiconducting polymers: the third generation. Chem Soc Rev. 2010; 39:2354–71. [PubMed: 20571667]
26. Wu Y, Zhu W. Organic sensitizers from D-π-A to D-A-π-A: effect of the internal electron-withdrawing units on molecular absorption, energy levels and photovoltaic performances. Chem Soc Rev. 2013; 42:2039–58. [PubMed: 23192709]
27. Wu C, Bull B, Christensen K, McNeill J. Ratiometric single-nanoparticle oxygen sensors for biological imaging. Angew Chem, Int Ed. 2009; 48:2741–5.
28. Tuncel D, Demir HV. Conjugated polymer nanoparticles. Nanoscale. 2010; 2:484–94. [PubMed: 20644748]
29. Wu C, Szymanski C, McNeill J. Preparation and encapsulation of highly fluorescent conjugated polymer nanoparticles. Langmuir. 2006; 22:2956–60. [PubMed: 16548540]
30. Feng L, Zhu C, Yuan H, Liu L, Lv F, Wang S. Conjugated polymer nanoparticles: preparation, properties, functionalization and biological applications. Chem Soc Rev. 2013; 42:6620–33. [PubMed: 23744297]
31. Wu P-J, Chen J-L, Chen C-P, Chan Y-H. Photoactivated ratiometric copper (II) ion sensing with semiconducting polymer dots. Chem Commun. 2013; 49:898–900.
32. Chan Y-H, Wu C, Ye F, Jin Y, Smith PB, Chiu DT. Development of ultrabright semiconducting polymer dots for ratiometric pH sensing. Anal Chem. 2011; 83:1448–55. [PubMed: 21244093]
33. Zhang P, Lu H, Chen H, Zhang J, Liu L, Lv F, et al. Cationic conjugated polymers-induced quorum sensing of bacteria cells. Anal Chem. 2016; 88:2985–8. [PubMed: 26912099]
34. Wu P-J, Kuo S-Y, Huang Y-C, Chen C-P, Chan Y-H. Polydiacetylene-enclosed near-infrared fluorescent semiconducting polymer dots for bioimaging and sensing. Anal Chem. 2014; 86:4831–9. [PubMed: 24749695]
35. Kim S, Lim C-K, Na J, Lee Y-D, Kim K, Choi K, et al. Conjugated polymer nanoparticles for biomedical in vivo imaging. Chem Commun. 2010; 46:1617–9.
36. Jeong K, Park S, Lee YD, Lim CK, Kim J, Chung BH, et al. Conjugated polymer/photochromophore binary nanococktails: bistable photoswitching of near-infrared fluorescence for in vivo imaging. Adv Mater. 2013; 25:5574–80. [PubMed: 23847108]
37. Wu C, Hansen SJ, Hou Q, Yu J, Zeigler M, Jin Y, et al. Design of highly emissive polymer dot bioconjugates for in vivo tumor targeting. Angew Chem, Int Ed. 2011; 50:3430–4.
38. Xiong L, Shuhendler AJ, Rao J. Self-luminescing BRET-FRET near-infrared dots for in vivo lymph-node mapping and tumour imaging. Nat Commun. 2012; 3:1193. [PubMed: 23149738]
39. Palner M, Pu K, Shao S, Rao J. Semiconducting polymer nanoparticles with persistent near-infrared luminescence for in vivo optical imaging. Angew Chem, Int Ed. 2015; 127:11639–42.
40. Zha Z, Deng Z, Li Y, Li C, Wang J, Wang S, et al. Biocompatible polypyrrole nanoparticles as a novel organic photoacoustic contrast agent for deep tissue imaging. Nanoscale. 2013; 5:4462–7. [PubMed: 23584573]
41. Cai X, Liu X, Liao LD, Bandla A, Ling JM, Liu YH, et al. Encapsulated conjugated oligomer nanoparticles for real-time photoacoustic sentinel lymph node imaging and targeted photothermal therapy. Small. 2016; 12:4873–80. [PubMed: 27439884]

42. Cheng L, He W, Gong H, Wang C, Chen Q, Cheng Z, et al. PEGylated micelle nanoparticles encapsulating a non-fluorescent near-infrared organic dye as a safe and highly-effective photothermal agent for in vivo cancer therapy. Adv Funct Mater. 2013; 23:5893–902.
43. Lyu Y, Xie C, Chechetka SA, Miyako E, Pu K. Semiconducting polymer nanobioconjugates for targeted photothermal activation of neurons. J Am Chem Soc. 2016; 138:9049–52. [PubMed: 27404507]
44. Zhang D, Wu M, Zeng Y, Liao N, Cai Z, Liu G, et al. Lipid micelles packaged with semiconducting polymer dots as simultaneous MRI/photoacoustic imaging and photodynamic/photothermal dual-modal therapeutic agents for liver cancer. J Mater Chem B. 2016; 4:589–99.
45. Yuan H, Wang B, Lv F, Liu L, Wang S. Conjugated-polymer-based energy-transfer systems for antimicrobial and anticancer applications. Adv Mater. 2014; 26:6978–82. [PubMed: 24711269]
46. Pu K, Chattopadhyay N, Rao J. Recent advances of semiconducting polymer nanoparticles in in vivo molecular imaging. J Controlled Release. 2016; 240:312–22.
47. Peng H-S, Chiu DT. Soft fluorescent nanomaterials for biological and biomedical imaging. Chem Soc Rev. 2015; 44:4699–722. [PubMed: 25531691]
48. Pecher J, Mecking S. Nanoparticles of conjugated polymers. Chem Rev. 2010; 110:6260–79. [PubMed: 20684570]
49. Pu KY, Liu B. Fluorescent conjugated polyelectrolytes for bioimaging. Adv Funct Mater. 2011; 21:3408–23.
50. Tian Z, Yu J, Wu C, Szymanski C, McNeill J. Amplified energy transfer in conjugated polymer nanoparticle tags and sensors. Nanoscale. 2010; 2:1999–2011. [PubMed: 20697652]
51. Li K, Liu B. Polymer-encapsulated organic nanoparticles for fluorescence and photoacoustic imaging. Chem Soc Rev. 2014; 43:6570–97. [PubMed: 24792930]
52. Massey M, Wu M, Conroy EM, Algar WR. Mind your P's and Q's: the coming of age of semiconducting polymer dots and semiconductor quantum dots in biological applications. Curr Opin Biotechnol. 2015; 34:30–40. [PubMed: 25481436]
53. Chan YH, Wu PJ. Semiconducting polymer nanoparticles as fluorescent probes for biological imaging and sensing. Part Part Syst Charact. 2015; 32:11–28.
54. Hashim Z, Howes P, Green M. Luminescent quantum-dot-sized conjugated polymer nanoparticles-nanoparticle formation in a miniemulsion system. J Mater Chem. 2011; 21:1797–803.
55. Kaeser A, Schenning AP. Fluorescent nanoparticles based on self-assembled π-conjugated systems. Adv Mater. 2010; 22:2985–97. [PubMed: 20535737]
56. Wu C, Bull B, Szymanski C, Christensen K, McNeill J. Multicolor conjugated polymer dots for biological fluorescence imaging. ACS Nano. 2008; 2:2415–23. [PubMed: 19206410]
57. Chen C-P, Wu P-J, Liou S-Y, Chan Y-H. Ultrabright benzoselenadiazole-based semiconducting polymer dots for specific cellular imaging. RSC Adv. 2013; 3:17507–14.
58. Davis CM, Childress ES, Harbron EJ. Ensemble and single-particle fluorescence photomodulation in diarylethene-doped conjugated polymer nanoparticles. J Phys Chem B. 2011; 115:19065–73.
59. Harbron EJ, Davis CM, Campbell JK, Allred RM, Kovary MT, Economou NJ. Photochromic dye-doped conjugated polymer nanoparticles: photomodulated emission and nanoenvironmental characterization. J Phys Chem C. 2009; 113:13707–14.
60. Howes P, Green M, Levitt J, Suhling K, Hughes M. Phospholipid encapsulated semiconducting polymer nanoparticles: their use in cell imaging and protein attachment. J Am Chem Soc. 2010; 132:3989–96. [PubMed: 20175539]
61. Vieira OV, Botelho RJ, Grinstein S. Phagosome maturation: aging gracefully. Biochem J. 2002; 366:689–704. [PubMed: 12061891]
62. Childress ES, Roberts CA, Sherwood DY, LeGuyader CL, Harbron EJ. Ratiometric fluorescence detection of mercury ions in water by conjugated polymer nanoparticles. Anal Chem. 2012; 84:1235–9. [PubMed: 22280026]
63. Rong Y, Wu C, Yu J, Zhang X, Ye F, Zeigler M, et al. Multicolor fluorescent semiconducting polymer dots with narrow emissions and high brightness. ACS Nano. 2013; 7:376–84. [PubMed: 23282278]

64. Ahmed E, Morton SW, Hammond PT, Swager TM. Fluorescent multiblock π-conjugated polymer nanoparticles for in vivo tumor targeting. Adv Mater. 2013; 25:4504–10. [PubMed: 23794490]
65. Ding D, Liu J, Feng G, Li K, Hu Y, Liu B. Bright far-red/near-infrared conjugated polymer nanoparticles for in vivo bioimaging. Small. 2013; 9:3093–102. [PubMed: 23625815]
66. Torabi M, Aquino SL, Harisinghani MG. Current concepts in lymph node imaging. J Nucl Med. 2004; 45:1509–18. [PubMed: 15347718]
67. Chen D, Wu I-C, Liu Z, Tang Y, Chen H, Yu J, et al. Semiconducting polymer dots with bright narrow-band emission at 800 nm for biological applications. Chem Sci. 2017; 8:3390–8. [PubMed: 28507710]
68. Oh MH, Lee N, Kim H, Park SP, Piao Y, Lee J, et al. Large-scale synthesis of bioinert tantalum oxide nanoparticles for X-ray computed tomography imaging and bimodal image-guided sentinel lymph node mapping. J Am Chem Soc. 2011; 133:5508–15. [PubMed: 21428437]
69. Erogbogbo F, Yong K-T, Roy I, Hu R, Law W-C, Zhao W, et al. In vivo targeted cancer imaging, sentinel lymph node mapping and multi-channel imaging with biocompatible silicon nanocrystals. ACS Nano. 2010; 5:413–23. [PubMed: 21138323]
70. Ravizzini G, Turkbey B, Barrett T, Kobayashi H, Choyke PL. Nanoparticles in sentinel lymph node mapping. Wiley Interdiscip Rev: Nanomed Nanobiotechnol. 2009; 1:610–23. [PubMed: 20049820]
71. Akers WJ, Kim C, Berezin M, Guo K, Fuhrhop R, Lanza GM, et al. Noninvasive photoacoustic and fluorescence sentinel lymph node identification using dye-loaded perfluorocarbon nanoparticles. ACS Nano. 2010; 5:173–82. [PubMed: 21171567]
72. Noh Y-W, Kong S-H, Choi D-Y, Park HS, Yang H-K, Lee H-J, et al. Near-infrared emitting polymer nanogels for efficient sentinel lymph node mapping. ACS Nano. 2012; 6:7820–31. [PubMed: 22862428]
73. Ballou B, Ernst LA, Andreko S, Harper T, Fitzpatrick JA, Waggoner AS, et al. Sentinel lymph node imaging using quantum dots in mouse tumor models. Bioconjugate Chem. 2007; 18:389–96.
74. Kim S, Lim YT, Soltesz EG, De Grand AM, Lee J, Nakayama A, et al. Near-infrared fluorescent type II quantum dots for sentinel lymph node mapping. Nat Biotechnol. 2004; 22:93–7. [PubMed: 14661026]
75. Zhu H, Fang Y, Zhen X, Wei N, Gao Y, Luo KQ, et al. Multilayered semiconducting polymer nanoparticles with enhanced NIR fluorescence for molecular imaging in cells, zebrafish and mice. Chem Sci. 2016; 7:5118–25.
76. Chow EK-H, Ho D. Cancer nanomedicine: from drug delivery to imaging. Sci Transl Med. 2013; 5:216rv4.
77. Shi L, Sordillo LA, Rodríguez-Contreras A, Alfano R. Transmission in near-infrared optical windows for deep brain imaging. J Biophotonics. 2016; 9:38–43. [PubMed: 26556561]
78. De Vries IJM, Lesterhuis WJ, Barentsz JO, Verdijk P, van Krieken JH, Boerman OC, et al. Magnetic resonance tracking of dendritic cells in melanoma patients for monitoring of cellular therapy. Nat Biotechnol. 2005; 23:1407. [PubMed: 16258544]
79. Pu K, Shuhendler AJ, Valta MP, Cui L, Saar M, Peehl DM, et al. Phosphorylcholine-coated semiconducting polymer nanoparticles as rapid and efficient labeling agents for in vivo cell tracking. Adv Healthcare Mater. 2014; 3:1292–8.
80. Ke C-S, Fang C-C, Yan J-Y, Tseng P-J, Pyle JR, Chen C-P, et al. Molecular engineering and design of semiconducting polymer dots with narrow-band, near-infrared emission for in vivo biological imaging. ACS Nano. 2017; 11:3166–77. [PubMed: 28221751]
81. Kang B, Li J, Chang S, Dai M, Ren C, Dai Y, et al. Subcellular tracking of drug release from carbon nanotube vehicles in living cells. Small. 2012; 8:777–82. [PubMed: 22223491]
82. Yu J-C, Chen Y-L, Zhang Y-Q, Yao X-K, Qian C-G, Huang J, et al. pH-responsive and near-infrared-emissive polymer nanoparticles for simultaneous delivery, release, and fluorescence tracking of doxorubicin in vivo. Chem Commun. 2014; 50:4699–702.
83. Atashi F, Modarressi A, Pepper MS. The role of reactive oxygen species in mesenchymal stem cell adipogenic and osteogenic differentiation: a review. Stem Cells Dev. 2015; 24:1150–63. [PubMed: 25603196]

84. Shi H, Ma X, Zhao Q, Liu B, Qu Q, An Z, et al. Ultrasmall phosphorescent polymer dots for ratiometric oxygen sensing and photodynamic cancer therapy. Adv Funct Mater. 2014; 24:4823–30.
85. Pu K, Shuhendler AJ, Rao J. Semiconducting polymer nanoprobe for in vivo imaging of reactive oxygen and nitrogen species. Angew Chem, Int Ed. 2013; 52:10325–9.
86. Yin C, Zhu H, Xie C, Zhang L, Chen P, Fan Q, et al. Organic nanoprobe cocktails for multilocal and multicolor fluorescence imaging of reactive oxygen species. Adv Funct Mater. 2017; 27:1700493.
87. Wu L, Wu I-C, DuFort CC, Carlson MA, Wu X, Chen L, et al. Photostable ratiometric pdot probe for in vitro and in vivo imaging of hypochlorous acid. J Am Chem Soc. 2017; 139:6911–8. [PubMed: 28459559]
88. Waldron-Lynch F, Herold KC. Continuous glucose monitoring: long live the revolution! Nat Clin Pract Endocrinol Metab. 2009; 5:82–3. [PubMed: 19092785]
89. Sun K, Tang Y, Li Q, Yin S, Qin W, Yu J, et al. In vivo dynamic monitoring of small molecules with implantable polymer-dot transducer. ACS Nano. 2016; 10:6769–81. [PubMed: 27303785]
90. Roda A, Pasini P, Mirasoli M, Michelini E, Guardigli M. Biotechnological applications of bioluminescence and chemiluminescence. Trends Biotechnol. 2004; 22:295–303. [PubMed: 15158059]
91. Zong C, Wu J, Liu M, Yang L, Yan F, Ju H. Chemiluminescence imaging for a protein assay via proximity-dependent DNAzyme formation. Anal Chem. 2014; 86:9939–44. [PubMed: 25181362]
92. Bi S, Ji B, Zhang Z, Zhang S. A chemiluminescence imaging array for the detection of cancer cells by dual-aptamer recognition and bio-bar-code nanoprobe-based rolling circle amplification. Chem Commun. 2013; 49:3452–4.
93. Wang Z, Li J, Liu B, Hu J, Yao X, Li J. Chemiluminescence of CdTe nanocrystals induced by direct chemical oxidation and its size-dependent and surfactant-sensitized effect. J Phys Chem B. 2005; 109:23304–11. [PubMed: 16375298]
94. Zhao S, Huang Y, Liu R, Shi M, Liu YM. A nonenzymatic chemiluminescent reaction enabling chemiluminescence resonance energy transfer to quantum dots. Chem -Eur J. 2010; 16:6142–5. [PubMed: 20411550]
95. Roda A, Guardigli M. Analytical chemiluminescence and bioluminescence: latest achievements and new horizons. Anal Bioanal Chem. 2012; 402:69–76. [PubMed: 22002591]
96. Shuhendler AJ, Pu K, Cui L, Uetrecht JP, Rao J. Real-time imaging of oxidative and nitrosative stress in the liver of live animals for drug-toxicity testing. Nat Biotechnol. 2014; 32:373–80. [PubMed: 24658645]
97. Zhen X, Zhang C, Xie C, Miao Q, Lim KL, Pu K. Intraparticle energy level alignment of semiconducting polymer nanoparticles to amplify chemiluminescence for ultrasensitive in vivo imaging of reactive oxygen species. ACS Nano. 2016; 10:6400–9. [PubMed: 27299477]
98. Seo YH, Singh A, Cho H-J, Kim Y, Heo J, Lim C-K, et al. Rational design for enhancing inflammation-responsive in vivo chemiluminescence via nanophotonic energy relay to near-infrared AIE-active conjugated polymer. Biomaterials. 2016; 84:111–8. [PubMed: 26826300]
99. Sekiya M, Umezawa K, Sato A, Citterio D, Suzuki K. A novel luciferin-based bright chemiluminescent probe for the detection of reactive oxygen species. Chem Commun. 2009:3047–9.
100. Teranishi K, Nishiguchi T. Cyclodextrin-bound 6-(4-methoxyphenyl) imidazo [1, 2-α] pyrazin-3 (7H)-ones with fluorescein as green chemiluminescent probes for superoxide anions. Anal Biochem. 2004; 325:185–95. [PubMed: 14751253]
101. Li P, Liu L, Xiao H, Zhang W, Wang L, Tang B. A new polymer nanoprobe based on chemiluminescence resonance energy transfer for ultrasensitive imaging of intrinsic superoxide anion in mice. J Am Chem Soc. 2016; 138:2893–6. [PubMed: 26908223]
102. Moon H, Kumar D, Kim H, Sim C, Chang J-H, Kim J-M, et al. Amplified photoacoustic performance and enhanced photothermal stability of reduced graphene oxide coated gold nanorods for sensitive photoacoustic imaging. ACS Nano. 2015; 9:2711–9. [PubMed: 25751167]

103. Li W, Rong P, Yang K, Huang P, Sun K, Chen X. Semimetal nanomaterials of antimony as highly efficient agent for photoacoustic imaging and photothermal therapy. Biomaterials. 2015; 45:18–26. [PubMed: 25662491]
104. Maji SK, Sreejith S, Joseph J, Lin M, He T, Tong Y, et al. Upconversion nanoparticles as a contrast agent for photoacoustic imaging in live mice. Adv Mater. 2014; 26:5633–8. [PubMed: 24913756]
105. Weber J, Beard PC, Bohndiek SE. Contrast agents for molecular photoacoustic imaging. Nat Methods. 2016; 13:639–50. [PubMed: 27467727]
106. Wang X, Pang Y, Ku G, Xie X, Stoica G, Wang L. Noninvasive laser-induced photoacoustic tomography for structural and functional in vivo imaging of the brain. Nat Biotechnol. 2003; 21:803–6. [PubMed: 12808463]
107. Kim C, Favazza C, Wang LV. In vivo photoacoustic tomography of chemicals: high-resolution functional and molecular optical imaging at new depths. Chem Rev. 2010; 110:2756–82. [PubMed: 20210338]
108. Ku G, Zhou M, Song S, Huang Q, Hazle J, Li C. Copper sulfide nanoparticles as a new class of photoacoustic contrast agent for deep tissue imaging at 1064 nm. ACS Nano. 2012; 6:7489–96. [PubMed: 22812694]
109. Hu S, Maslov K, Wang LV. Second-generation optical-resolution photoacoustic microscopy with improved sensitivity and speed. Opt Lett. 2011; 36:1134–6. [PubMed: 21479007]
110. Wang C, Bao C, Liang S, Fu H, Wang K, Deng M, et al. RGD-conjugated silica-coated gold nanorods on the surface of carbon nanotubes for targeted photoacoustic imaging of gastric cancer. Nanoscale Res Lett. 2014; 9:264. [PubMed: 24948888]
111. Yang H-W, Liu H-L, Li M-L, Hsi I-W, Fan C-T, Huang C-Y, et al. Magnetic gold-nanorod/PNIPAAmMA nanoparticles for dual magnetic resonance and photoacoustic imaging and targeted photothermal therapy. Biomaterials. 2013; 34:5651–60. [PubMed: 23602366]
112. Padmanabhan P, Kumar A, Kumar S, Chaudhary RK, Gulyás B. Nanoparticles in practice for molecular-imaging applications: An overview. Acta Biomater. 2016; 41:1–16. [PubMed: 27265153]
113. Xie L, Wang G, Zhou H, Zhang F, Guo Z, Liu C, et al. Functional long circulating single walled carbon nanotubes for fluorescent/photoacoustic imaging-guided enhanced phototherapy. Biomaterials. 2016; 103:219–28. [PubMed: 27392290]
114. Lovell JF, Jin CS, Huynh E, Jin H, Kim C, Rubinstein JL, et al. Porphysome nanovesicles generated by porphyrin bilayers for use as multimodal biophotonic contrast agents. Nat Mater. 2011; 10:324–32. [PubMed: 21423187]
115. Huang P, Lin J, Wang X, Wang Z, Zhang C, He M, et al. Light-triggered theranostics based on photosensitizer-conjugated carbon dots for simultaneous enhanced-fluorescence imaging and photodynamic therapy. Adv Mater. 2012; 24:5104–10. [PubMed: 22718562]
116. Lyu Y, Fang Y, Miao Q, Zhen X, Ding D, Pu K. Intraparticle molecular orbital engineering of semiconducting polymer nanoparticles as amplified theranostics for in vivo photoacoustic imaging and photothermal therapy. ACS Nano. 2016; 10:4472–81. [PubMed: 26959505]
117. Cui D, Xie C, Pu K. Development of semiconducting polymer nanoparticles for photoacoustic imaging. Macromol Rapid Commun. 2017; 38:1700125.
118. Jiang Y, Pu K. Advanced photoacoustic imaging applications of near-infrared absorbing organic nanoparticles. Small. 2017; 13:1700710.
119. Miao Q, Pu K. Emerging designs of activatable photoacoustic probes for molecular imaging. Bioconjugate Chem. 2016; 27:2808–23.
120. Cui L, Rao J. Semiconducting polymer nanoparticles as photoacoustic molecular imaging probes. WIREs Nanomed Nanobiotechnol. 2017; 9:e1418.
121. Pu K, Mei J, Jokerst JV, Hong G, Antaris AL, Chattopadhyay N, et al. Diketopyrrolopyrrole-based semiconducting polymer nanoparticles for in vivo photoacoustic imaging. Adv Mater. 2015; 27:5184–90. [PubMed: 26247171]
122. Stahl T, Bofinger R, Lam I, Fallon KJ, Johnson P, Ogunlade O, et al. Tunable semiconducting polymer nanoparticles with INDT-based conjugated polymers for photoacoustic molecular imaging. Bioconjugate Chem. 2017; 28:1734–40.

123. Pu K, Shuhendler AJ, Jokerst JV, Mei J, Gambhir SS, Bao Z, et al. Semiconducting polymer nanoparticles as photoacoustic molecular imaging probes in living mice. Nat Nanotechnol. 2014; 9:233–9. [PubMed: 24463363]

124. Purushotham AD, Upponi S, Klevesath MB, Bobrow L, Millar K, Myles JP, et al. Morbidity after sentinel lymph node biopsy in primary breast cancer: results from a randomized controlled trial. J Clin Oncol. 2005; 23:4312–21. [PubMed: 15994144]

125. Veronesi U, Paganelli G, Viale G, Luini A, Zurrida S, Galimberti V, et al. A randomized comparison of sentinel-node biopsy with routine axillary dissection in breast cancer. N Engl J Med. 2003; 349:546–53. [PubMed: 12904519]

126. Zhang J, Yang S, Ji X, Zhou Q, Xing D. Characterization of lipid-rich aortic plaques by intravascular photoacoustic tomography. J Am Coll Cardiol. 2014; 64:385–90. [PubMed: 25060374]

127. Zhang J, Chen H, Zhou T, Wang L, Gao D, Zhang X, et al. A PIID-DTBT based semiconducting polymer dot with broad and strong optical absorption in the visible-light region as a highly-effective contrast agent for multiscale and multi-spectral photoacoustic imaging. Nano Res. 2016; 10:64–76.

128. Liu J, Geng J, Liao L-D, Thakor N, Gao X, Liu B. Conjugated polymer nanoparticles for photoacoustic vascular imaging. Poly Chem. 2014; 5:2854–62.

129. Jiang Y, Upputuri PK, Xie C, Lyu Y, Zhang L, Xiong Q, et al. Broadband absorbing semiconducting polymer nanoparticles for photoacoustic imaging in second near-infrared window. Nano Lett. 2017; 17:4964–9. [PubMed: 28654292]

130. Xie C, Upputuri PK, Zhen X, Pramanik M, Pu K. Self-quenched semiconducting polymer nanoparticles for amplified in vivo photoacoustic imaging. Biomaterials. 2017; 119:1–8. [PubMed: 27988405]

131. Zhen X, Feng X, Xie C, Zheng Y, Pu K. Surface engineering of semiconducting polymer nanoparticles for amplified photoacoustic imaging. Biomaterials. 2017; 127:97–106. [PubMed: 28284105]

132. Rijcken CJ, Snel CJ, Schiffelers RM, van Nostrum CF, Hennink WE. Hydrolysable core-crosslinked thermosensitive polymeric micelles: synthesis, characterisation and in vivo studies. Biomaterials. 2007; 28:5581–93. [PubMed: 17915312]

133. Cui D, Xie C, Lyu Y, Zhen X, Pu K. Near-infrared absorbing amphiphilic semiconducting polymers for photoacoustic imaging. J Mater Chem B. 2017; 5:4406–9.

134. Yin C, Zhen X, Zhao H, Tang Y, Ji Y, Lyu Y, et al. Amphiphilic semiconducting oligomer for near-infrared photoacoustic and fluorescence imaging. ACS Appl Mater Interfaces. 2017; 9:12332–9. [PubMed: 28299923]

135. Xie C, Zhen X, Lei Q, Ni R, Pu K. Self-assembly of semiconducting polymer amphiphiles for in vivo photoacoustic imaging. Adv Funct Mater. 2017; 27:1605397.

136. Zhang J, Zhen X, Upputuri PK, Pramanik M, Chen P, Pu K. Activatable photoacoustic nanoprobes for in vivo ratiometric imaging of peroxynitrite. Adv Mater. 2017; 29:1604764.

137. Yin C, Zhen X, Fan Q, Huang W, Pu K. Degradable semiconducting oligomer amphiphile for ratiometric photoacoustic imaging of hypochlorite. ACS Nano. 2017; 11:4174–82. [PubMed: 28296388]

138. Lee N, Hummer DR, Sverjensky DA, Rajh T, Hazen RM, Steele A, et al. Speciation of l-DOPA on nanorutile as a function of pH and surface coverage using Surface-Enhanced Raman Spectroscopy (SERS). Langmuir. 2012; 28:17322–30. [PubMed: 23163294]

139. Coakley RJ, Taggart C, McElvaney NG, O'Neill SJ. Cytosolic pH and the inflammatory microenvironment modulate cell death in human neutrophils after phagocytosis. Blood. 2002; 100:3383–91. [PubMed: 12384441]

140. Webb BA, Chimenti M, Jacobson MP, Barber DL. Dysregulated pH: a perfect storm for cancer progression. Nat Rev Cancer. 2011; 11:671–7. [PubMed: 21833026]

141. Kong KV, Dinish U, Lau WKO, Olivo M. Sensitive SERS-pH sensing in biological media using metal carbonyl functionalized planar substrates. Biosens Bioelectron. 2014; 54:135–40. [PubMed: 24269755]

142. Miao Q, Lyu Y, Ding D, Pu K. Semiconducting oligomer nanoparticles as an activatable photoacoustic probe with amplified brightness for in vivo imaging of pH. Adv Mater. 2016; 28:3662–8. [PubMed: 27000431]

143. Furdui CM, Poole LB. Chemical approaches to detect and analyze protein sulfenic acids. Mass Spectrom Rev. 2014; 33:126–46. [PubMed: 24105931]

144. Paulsen CE, Carroll KS. Orchestrating redox signaling networks through regulatory cysteine switches. ACS Chem Biol. 2009; 5:47–62.

145. Seo YH, Carroll KS. Profiling protein thiol oxidation in tumor cells using sulfenic acid-specific antibodies. Proc Natl Acad Sci U S A. 2009; 106:16163–8. [PubMed: 19805274]

146. Gautier V, Le H-T, Malki A, Messaoudi N, Caldas T, Kthiri F, et al. YajL, the prokaryotic homolog of the Parkinsonism-associated protein DJ-1, protects cells against protein sulfenylation. J Mol Biol. 2012; 421:662–70. [PubMed: 22321799]

147. Lyu Y, Zhen X, Miao Y, Pu K. Reaction-based semiconducting polymer nanoprobes for photoacoustic imaging of protein sulfenic acids. ACS Nano. 2016; 11:358–67. [PubMed: 27997794]

148. Perrier A, Roy P-M, Aujesky D, Chagnon I, Howarth N, Gourdier A-L, et al. Diagnosing pulmonary embolism in outpatients with clinical assessment, D-dimer measurement, venous ultrasound, and helical computed tomography: a multicenter management study. Am J Med. 2004; 116:291–9. [PubMed: 14984813]

149. Cui C, Yang Z, Hu X, Wu J, Shou K, Ma H, et al. Organic semiconducting nanoparticles as efficient photoacoustic agents for lightening early thrombus and monitoring thrombolysis in living mice. ACS Nano. 2017; 11:3298–310. [PubMed: 28240881]

150. Li J, Cai R, Kawazoe N, Chen G. Facile preparation of albumin-stabilized gold nanostars for the targeted photothermal ablation of cancer cells. J Mater Chem B. 2015; 3:5806–14.

151. Wang S, Zhao J, Hu F, Li X, An X, Zhou S, et al. Phase-changeable and bubble-releasing implants for highly efficient HIFU-responsive tumor surgery and chemotherapy. J Mater Chem B. 2016; 4:7368–78.

152. Topalian SL, Taube JM, Anders RA, Pardoll DM. Mechanism-driven biomarkers to guide immune checkpoint blockade in cancer therapy. Nat Rev Cancer. 2016; 16:275–87. [PubMed: 27079802]

153. Zhang L, Zheng W, Tang R, Wang N, Zhang W, Jiang X. Gene regulation with carbon-based siRNA conjugates for cancer therapy. Biomaterials. 2016; 104:269–78. [PubMed: 27472164]

154. Qin S-Y, Zhang A-Q, Cheng S-X, Rong L, Zhang X-Z. Drug self-delivery systems for cancer therapy. Biomaterials. 2017; 112:234–47. [PubMed: 27768976]

155. Ahn J, Miura Y, Yamada N, Chida T, Liu X, Kim A, et al. Antibody fragment-conjugated polymeric micelles incorporating platinum drugs for targeted therapy of pancreatic cancer. Biomaterials. 2015; 39:23–30. [PubMed: 25477168]

156. Zhang Y, Zhang Y, Hong G, He W, Zhou K, Yang K, et al. Biodistribution, pharmacokinetics and toxicology of Ag2S near-infrared quantum dots in mice. Biomaterials. 2013; 34:3639–46. [PubMed: 23415643]

157. Khlebtsov N, Dykman L. Biodistribution and toxicity of engineered gold nanoparticles: a review of in vitro and in vivo studies. Chem Soc Rev. 2011; 40:1647–71. [PubMed: 21082078]

158. Hessel CM, Pattani VP, Rasch M, Panthani MG, Koo B, Tunnell JW, et al. Copper selenide nanocrystals for photothermal therapy. Nano Lett. 2011; 11:2560–6. [PubMed: 21553924]

159. Geng J, Sun C, Liu J, Liao LD, Yuan Y, Thakor N, et al. Biocompatible conjugated polymer nanoparticles for efficient photothermal tumor therapy. Small. 2015; 11:1603–10. [PubMed: 25367500]

160. Yang K, Xu H, Cheng L, Sun C, Wang J, Liu Z. In vitro and in vivo near-infrared photothermal therapy of cancer using polypyrrole organic nanoparticles. Adv Mater. 2012; 24:5586–92. [PubMed: 22907876]

161. Cheng L, Yang K, Chen Q, Liu Z. Organic stealth nanoparticles for highly effective in vivo near-infrared photothermal therapy of cancer. ACS Nano. 2012; 6:5605–13. [PubMed: 22616847]

162. Zhou J, Lu Z, Zhu X, Wang X, Liao Y, Ma Z, et al. NIR photothermal therapy using polyaniline nanoparticles. Biomaterials. 2013; 34:9584–92. [PubMed: 24044996]

163. Li S, Wang X, Hu R, Chen H, Li M, Wang J, et al. Near-infrared (NIR)-absorbing conjugated polymer dots as highly effective photothermal materials for in vivo cancer therapy. Chem Mater. 2016; 28:8669–75.
164. Li D-D, Wang J-X, Ma Y, Qian H-S, Wang D, Wang L, et al. A donor-acceptor conjugated polymer with alternating isoindigo derivative and bithiophene units for near-infrared modulated cancer thermo-chemotherapy. ACS Appl Mater Interfaces. 2016; 8:19312–20. [PubMed: 27404741]
165. Guo B, Feng G, Manghnani PN, Cai X, Liu J, Wu W, et al. A porphyrin-based conjugated polymer for highly efficient in vitro and in vivo photothermal therapy. Small. 2016; 12:6243–54. [PubMed: 27671747]
166. Huang Y, He S, Cao W, Cai K, Liang X-J. Biomedical nanomaterials for imaging-guided cancer therapy. Nanoscale. 2012; 4:6135–49. [PubMed: 22929990]
167. Lim EK, Huh YM, Yang J, Lee K, Suh JS, Haam S. pH-triggered drug-releasing magnetic nanoparticles for cancer therapy guided by molecular imaging by MRI. Adv Mater. 2011; 23:2436–42. [PubMed: 21491515]
168. Huang P, Bao L, Zhang C, Lin J, Luo T, Yang D, et al. Folic acid-conjugated silica-modified gold nanorods for X-ray/CT imaging-guided dual-mode radiation and photo-thermal therapy. Biomaterials. 2011; 32:9796–809. [PubMed: 21917309]
169. Yu MK, Kim D, Lee IH, So JS, Jeong YY, Jon S. Image-guided prostate cancer therapy using aptamer-functionalized thermally cross-linked superparamagnetic iron oxide nanoparticles. Small. 2011; 7:2241–9. [PubMed: 21648076]
170. Lin J, Wang S, Huang P, Wang Z, Chen S, Niu G, et al. Photosensitizer-loaded gold vesicles with strong plasmonic coupling effect for imaging-guided photothermal/photodynamic therapy. ACS Nano. 2013; 7:5320–9. [PubMed: 23721576]
171. Li J, Shi X, Shen M. Hydrothermal synthesis and functionalization of iron oxide nanoparticles for MR imaging applications. Part Part Syst Charact. 2014; 31:1223–37.
172. Zhang J, Yang C, Zhang R, Chen R, Zhang Z, Zhang W, et al. Biocompatible D-A semiconducting polymer nanoparticle with light-harvesting unit for highly effective photoacoustic imaging guided photothermal therapy. Adv Funct Mater. 2017; 27:1605094. [PubMed: 29046623]
173. Yang Z, Tian R, Wu J, Fan Q, Yung BC, Niu G, et al. Impact of semiconducting perylene diimide nanoparticle size on lymph node mapping and cancer imaging. ACS Nano. 2017; 11:4247–55. [PubMed: 28345873]
174. Corbitt TS, Sommer JR, Chemburu S, Ogawa K, Ista LK, Lopez GP, et al. Conjugated polyelectrolyte capsules: light-activated antimicrobial micro “roach motels”. ACS Appl Mater Interfaces. 2008; 1:48–52.
175. Li S, Chang K, Sun K, Tang Y, Cui N, Wang Y, et al. Amplified singlet oxygen generation in semiconductor polymer dots for photodynamic cancer therapy. ACS Appl Mater Interfaces. 2015; 8:3624–34. [PubMed: 26492203]
176. Tang Y, Chen H, Chang K, Liu Z, Wang Y, Qu S, et al. Photo-cross-linkable polymer dots with stable sensitizer loading and amplified singlet oxygen generation for photodynamic therapy. ACS Appl Mater Interfaces. 2017; 9:3419–31. [PubMed: 28067486]
177. Chang K, Tang Y, Fang X, Yin S, Xu H, Wu C. Incorporation of porphyrin to π-conjugated backbone for polymer-dot-sensitized photodynamic therapy. Biomacromolecules. 2016; 17:2128–36. [PubMed: 27219282]
178. Guo L, Ge J, Liu Q, Jia Q, Zhang H, Liu W, et al. Versatile polymer nanoparticles as two-photon-triggered photosensitizers for simultaneous cellular, deep-tissue imaging, and photodynamic therapy. Adv Healthcare Mater. 2017; 6:1601431.
179. Chang K, Liu Z, Fang X, Chen H, Men X, Yuan Y, et al. Enhanced phototherapy by nanoparticle-enzyme via generation and photolysis of hydrogen peroxide. Nano Lett. 2017; 17:4323–9. [PubMed: 28613898]
180. Skovsen E, Snyder JW, Lambert JD, Ogilby PR. Lifetime and diffusion of singlet oxygen in a cell. J Phys Chem B. 2005; 109:8570–3. [PubMed: 16852012]

181. Kim S, Tachikawa T, Fujitsuka M, Majima T. Far-red fluorescence probe for monitoring singlet oxygen during photodynamic therapy. J Am Chem Soc. 2014; 136:11707–15. [PubMed: 25075870]

182. Gao S, Wang G, Qin Z, Wang X, Zhao G, Ma Q, et al. Oxygen-generating hybrid nanoparticles to enhance fluorescent/photoacoustic/ultrasound imaging guided tumor photodynamic therapy. Biomaterials. 2017; 112:324–35. [PubMed: 27776285]

183. He C, Liu D, Lin W. Self-assembled core-shell nanoparticles for combined chemotherapy and photodynamic therapy of resistant head and neck cancers. ACS Nano. 2015; 9:991–1003. [PubMed: 25559017]

184. Chen Q, Wang C, Cheng L, He W, Cheng Z, Liu Z. Protein modified upconversion nanoparticles for imaging-guided combined photothermal and photodynamic therapy. Biomaterials. 2014; 35:2915–23. [PubMed: 24412081]

185. Seo S-H, Kim B-M, Joe A, Han H-W, Chen X, Cheng Z, et al. NIR-light-induced surface-enhanced Raman scattering for detection and photothermal/photodynamic therapy of cancer cells using methylene blue-embedded gold nanorod@SiO_2 nanocomposites. Biomaterials. 2014; 35:3309–18. [PubMed: 24424205]

186. Feng G, Fang Y, Liu J, Geng J, Ding D, Liu B. Multifunctional conjugated polymer nanoparticles for image-guided photodynamic and photothermal therapy. Small. 2017; 13:1602807.

187. Cai Y, Liang P, Tang Q, Yang X, Si W, Huang W, et al. Diketopyrrolopyrrole-triphenylamine organic nanoparticles as multifunctional reagents for photoacoustic imaging-guided photodynamic/photothermal synergistic tumor therapy. ACS Nano. 2017; 11:1054–63. [PubMed: 28033465]

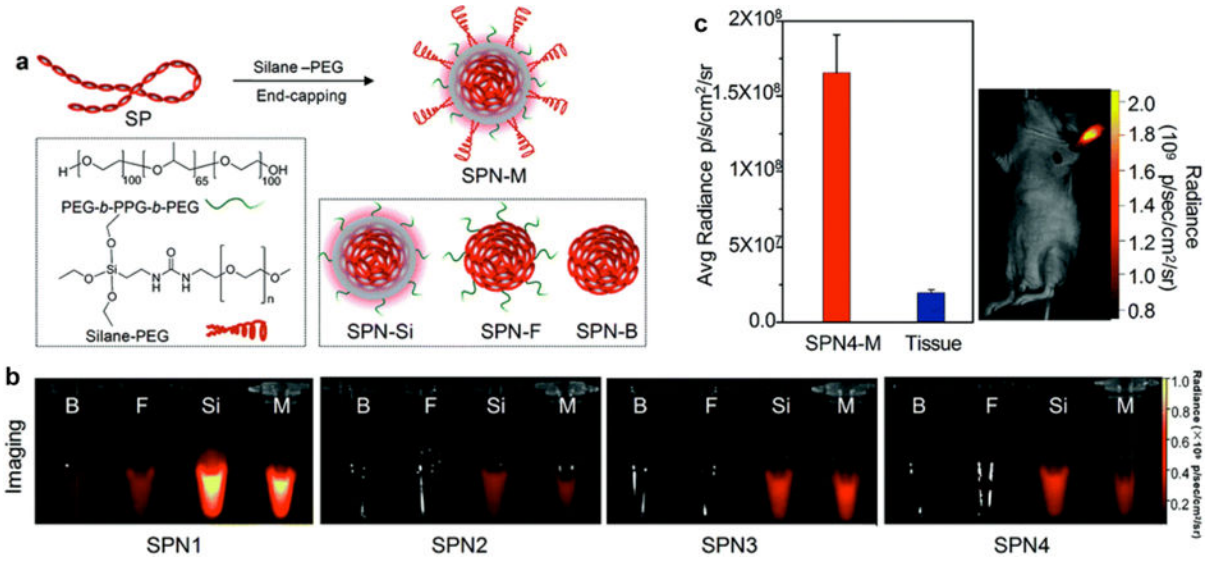

Fig. 1.

(a) Schematic illustration of the preparation of SPN-M. (b) IVIS fluorescence images of SPNs1-4 with indicated coatings. (c) Left: quantification of the fluorescence intensity of lymph nodes and normal tissue in living mice at 4 h after the intradermal injection of SPN4-M into the forepaw. Right: whole-body fluorescence imaging of a living mouse at 4 h after intradermal injection of SPN4-M (1 mg mL^{-1}, 30 μL) into the forepaw. Reprinted with permission from Ref. [75], copyright 2016, The Royal Society of Chemistry.

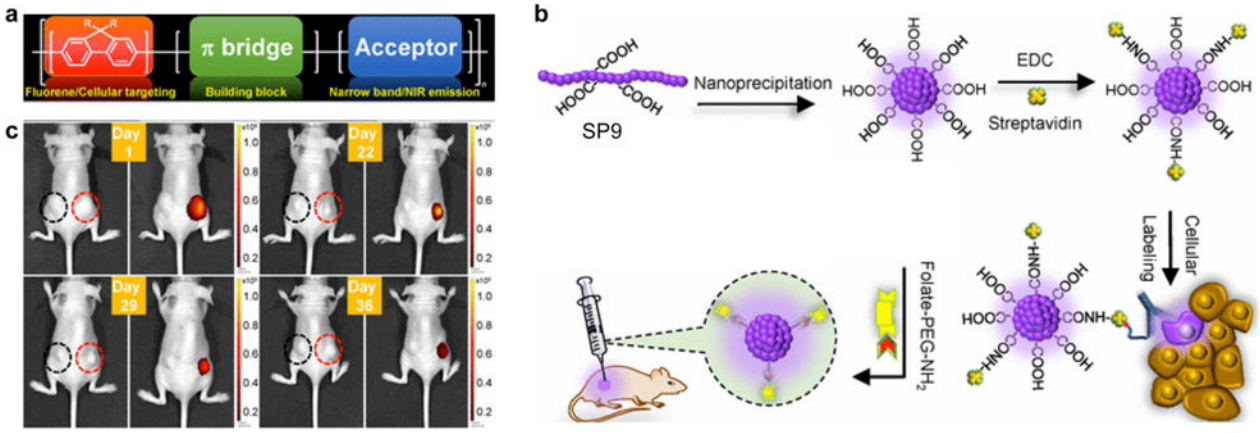

Fig. 2.

(a) Donor-bridge-acceptor structure of SPs. (b) Schematic diagram showing the preparation of carboxylic-acid-functionalized SPN9 and conjugation with biomolecules for the specific cellular targeting and *in vivo* bioimaging. (c) Time-dependent *in vivo* bright-field (left) and fluorescence (right) imaging of a mouse implanted SKOV-3 cells labeled with bare SPN9 (left black circle) or folic acid functionalized SPN9 (right red circle). Reprinted with permission from Ref. [80], copyright 2017, The Royal Society of Chemistry.

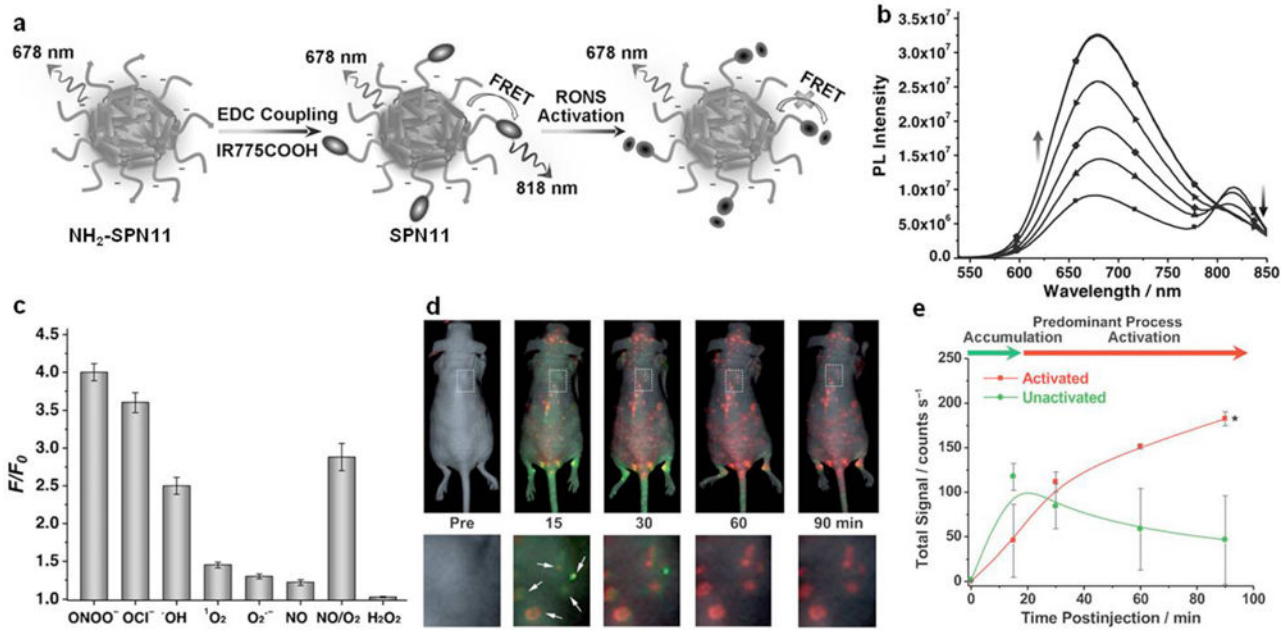

Fig. 3.

(a) Preparation and RONS sensing of SPN11. (b) Fluorescence spectra of SPN11 in the absence or presence of $ONOO^-$ at concentrations of 0.1, 0.2, 0.3, 0.4, or 0.5 μM. (c) Fluorescence responses of SPN11 (0.1 μg mL^{-1}) toward RONS in nitrogen-purged PBS (pH 7.4). F and F_0 stand for the fluorescence intensities at λ_{em} = 678 nm in the presence and absence of RONS (1 μM), respectively. Excitation at 405 nm. (d) Imaging RONS with SPN11 in mice with spontaneous systemic *C. bovis* bacterial infection. Overlaid images of activated (pseudo red) and unactivated (pseudo green) SPN11 following intravenous administration to mice with spontaneous infections. Enlargements of the regions indicated by dashed white boxes are given below each corresponding image. White arrows indicate localized regions of bacterial infection. (e) Quantification of activated (red) and nonactivated (green) SPN11 fluorescence over time. Reprinted with permission from Ref. [85], copyright 2013, WILEY-VCH Verlag GmbH & Co. KGaA, Weinheim.

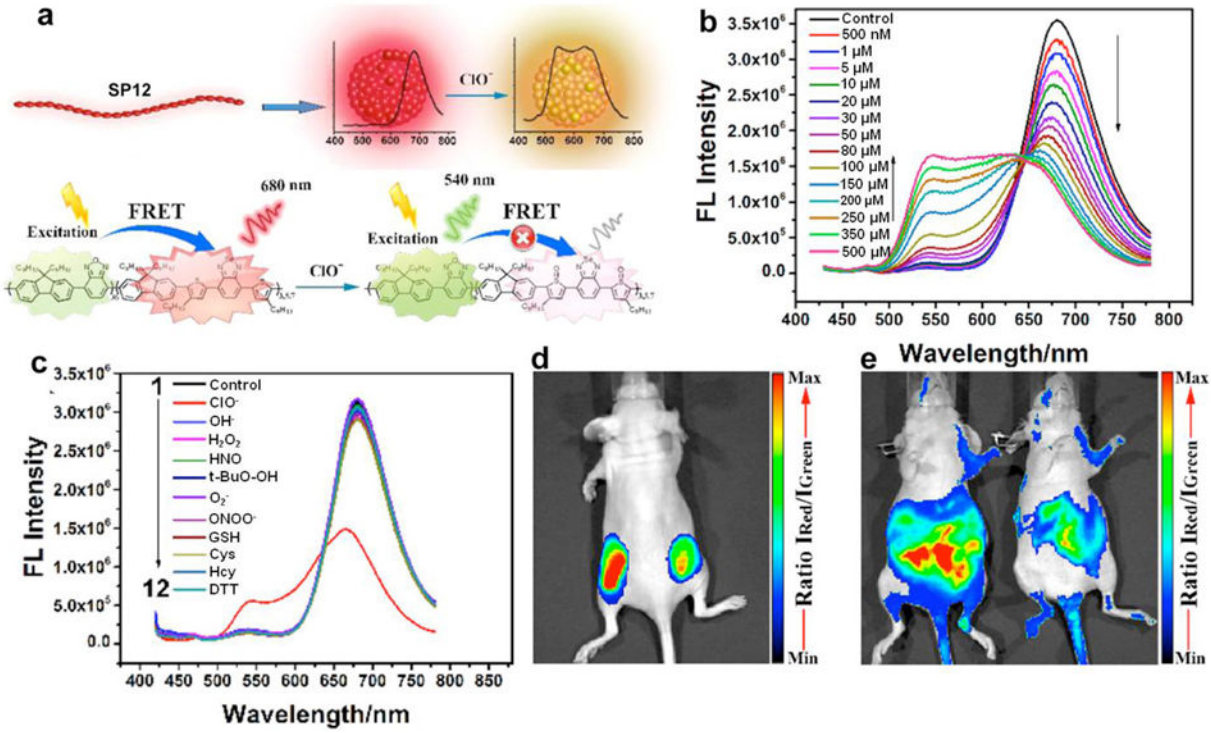

Fig. 4.

(a) Schematic illustration of SPN12 preparation by nanoprecipitation and ClO^- sensing. (b) Fluorescence performance of SPN12 in the presence of different concentrations of ClO^-. (c) Fluorescence spectra of SPN12 in the presence of various ROS and biologically relevant analytes. (d) *In vivo* imaging of exogenous ClO^- using SPN12. Representative ratiometric (pseudocolor) image of mouse with the subcutaneous implantation of SPN12 (left) and SPN12 + ClO^- (right). (e) *In vivo* imaging of endogenous ClO^- production from the peritoneal cavity of the mice with SPN12 during an LPS-mediated inflammatory response. Representative ratiometric images (pseudocolor) of mice intraperitoneally treated with saline (left) and LPS (right), followed by an intraperitoneal injection of SPN12 at 4 h later. Fluorescence images were acquired 30 min after the injection of SPN12 with a 465 nm excitation filter and 540 nm (green channel) and 680 nm (red channel) emission filters. Ratiometric images were obtained by pixel-by-pixel calculation using ImageJ software. Reprinted with permission from Ref. [87], copyright 2017, American Chemical Society.

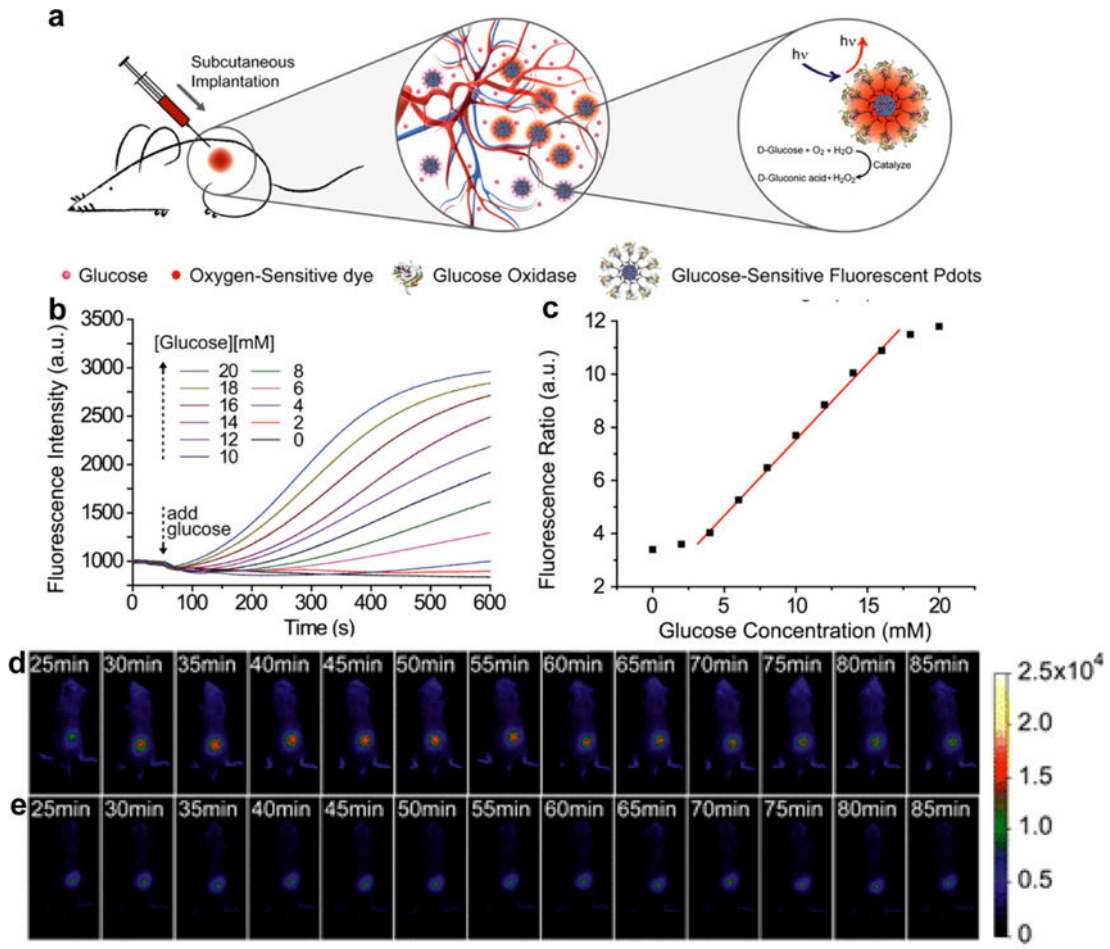

Fig. 5.

(a) Schematic illustration the *in vivo* glucose monitoring by using SPN13. (b) Response curves of SPN13 to glucose in aqueous suspensions. (c) Ratiometric calibration plot (I_{648}/I_{428}) of SPN13 sensor as a function of glucose concentration. *In vivo* fluorescence imaging of SPN13 injected living mouse with (d) and without (e) administration of glucose and insulin. Reprinted with permission from Ref. [89], copyright 2016, American Chemical Society.

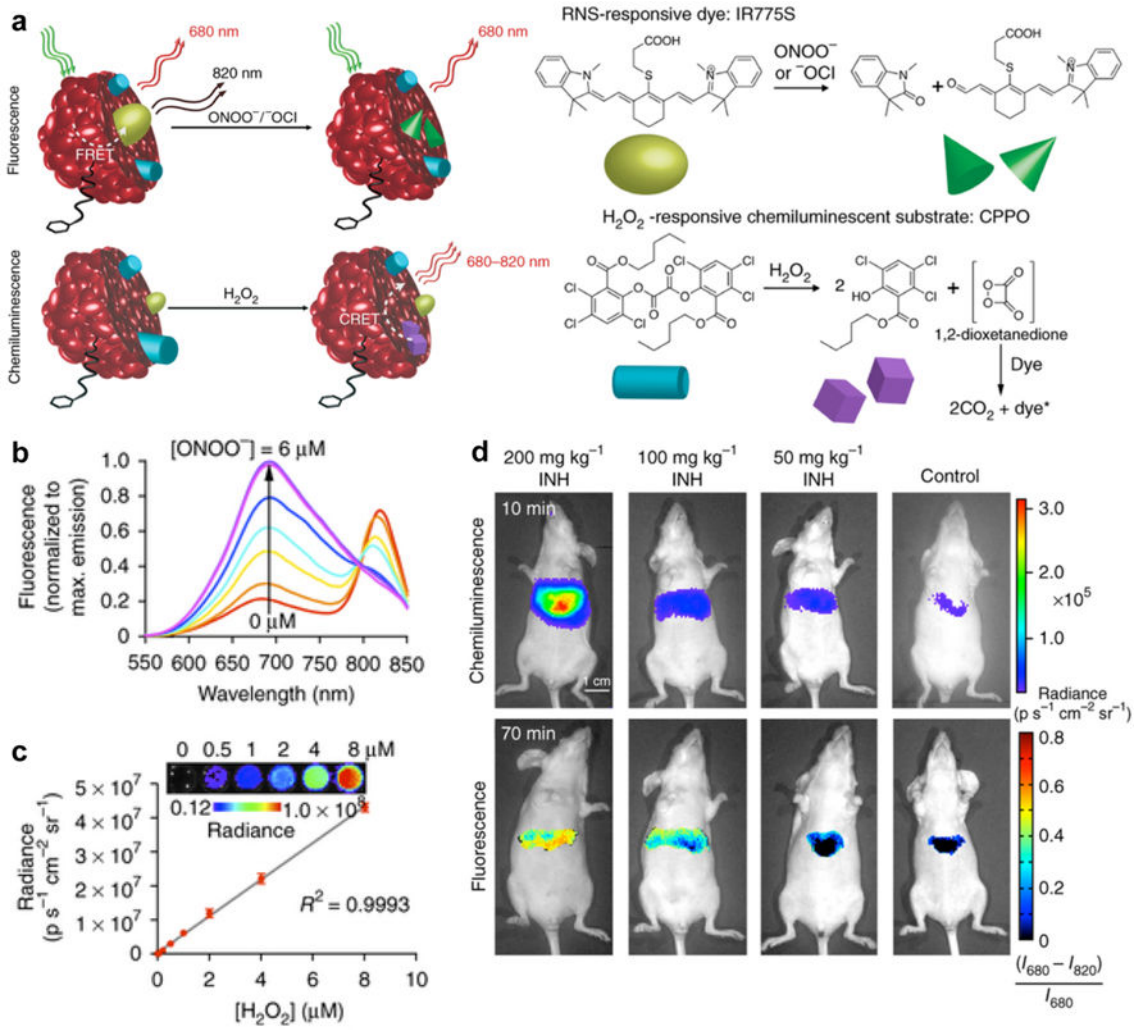

Fig. 6.

(a) Illustration of the mechanism of simultaneous and differential detection of $ONOO^-/^-OCl$ and H_2O_2 by SPN14. (b) Sensitivity and range of fluorescence ratiometric detection of $ONOO^-$ with SPN14 after incremental additions of NaONOO. (c) Chemiluminescence response of SPN14 to varying concentrations of H_2O_2. (d) Representative images of mice that received INH or saline (control) intraperitoneally followed by SPN14 injection. Reprinted with permission from Ref. [96], copyright 2014, Nature Publishing Group.

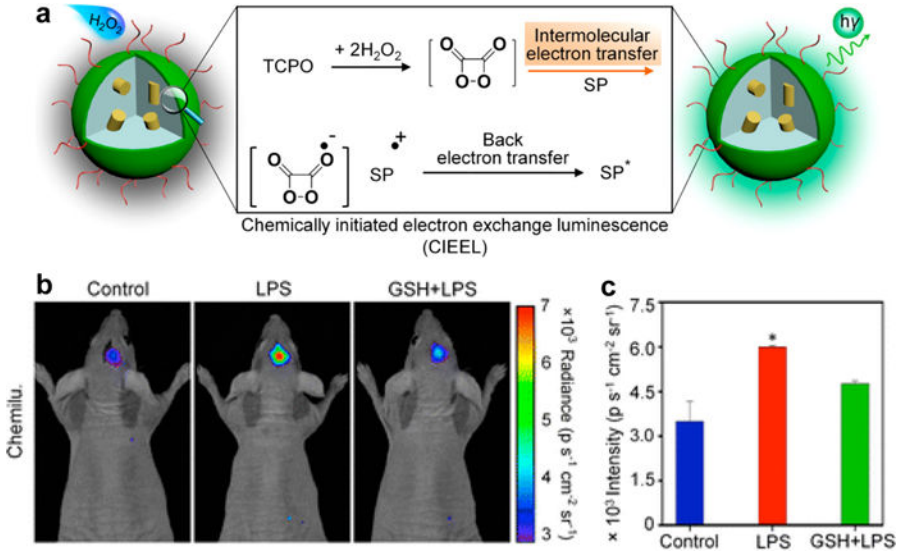

Fig. 7.

(a) Illustration of CIEEL mechanism of SPNs. (b) Representative *in vivo* chemiluminescence images of mice treated with saline, LPS or LPS with GSH, followed by intracerebral injection of SPN15 at t = 4 h later. Chemiluminescence was acquired at t = 1 min after SPN15 administration. (c) Quantification of chemiluminescence signal calculated from the *in vivo* images in (b). Reprinted with permission from Ref. [97], copyright 2016, American Chemical Society.

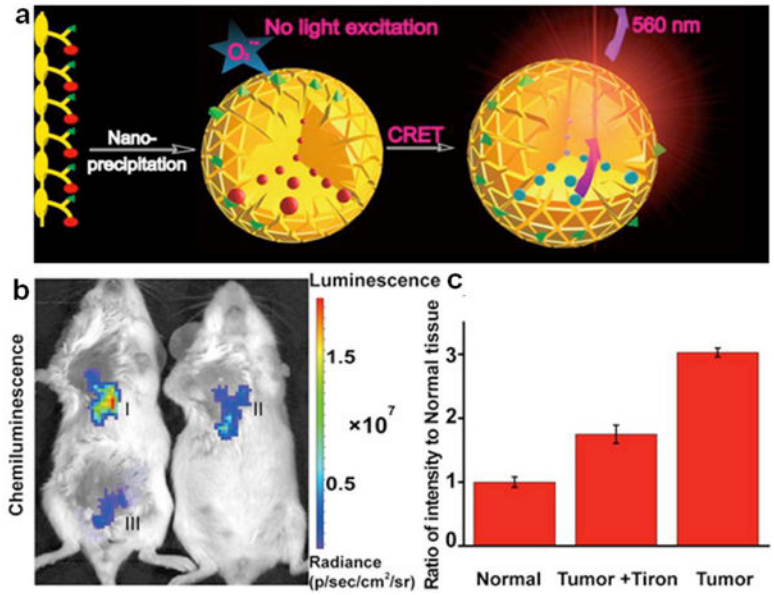

Fig. 8.

(a) Schematic illustration of SPN17 preparation by "nanoprecipitation" and $O_2^{\bullet}-$ sensing. (b) Representative images (pseudocolor) of mice *in vivo* tumor (I), tumor + Tiron (II) and normal (III) tissues followed by SPN17 administration. Images (λ_{em} = 570 ± 10 nm) were acquired using an IVIS Lumina II at 30 s after SPN17 administration. (c) Quantitative chemiluminescence intensities of (I-III). Reprinted with permission from Ref. [101], copyright 2016, American Chemical Society.

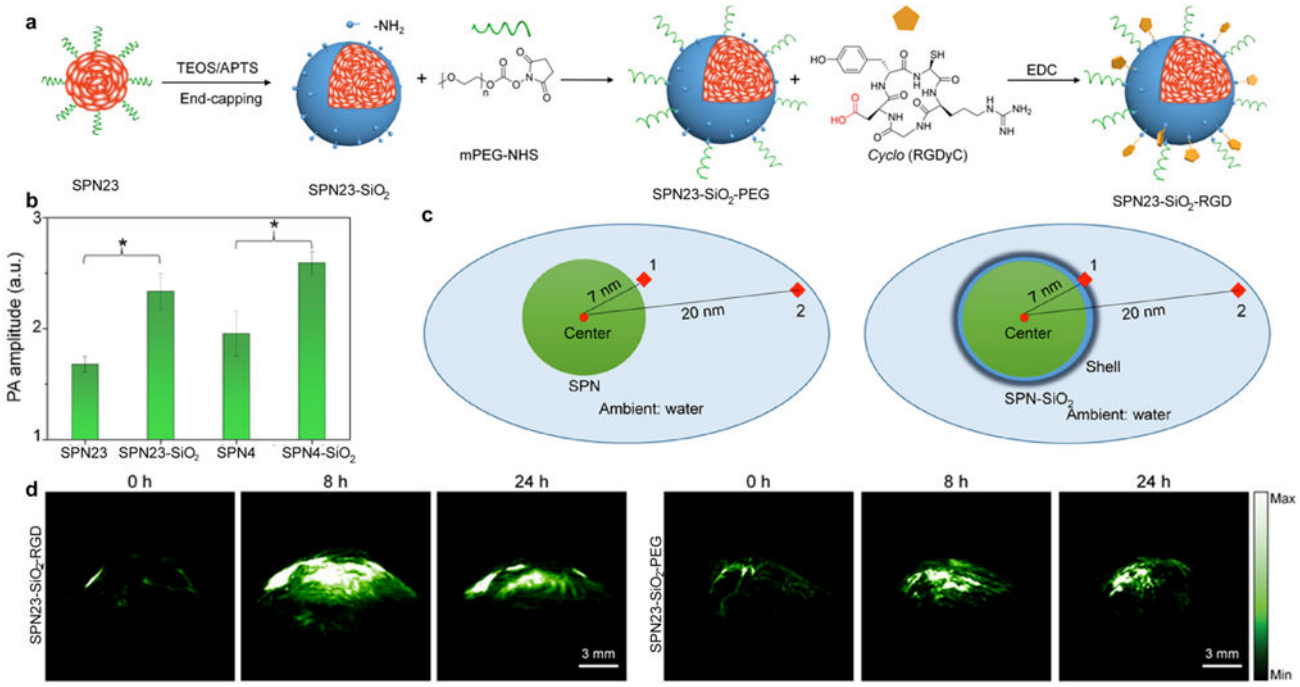

Fig. 9.

(a) Synthesis of SPN23-SiO_2-PEG and SPN23-SiO_2-RGD. (b) Comparison of PA amplitudes of SPN23 and SPN23-SiO_2 at 760 nm, and SPN4 and SPN4-SiO_2 at 680 nm under the same concentration. (c) Schematic illustration of the COMSOL simulation for SPNs. (1 and 2 are the two test points for measuring temperature and PA signal). (d) Representative PA images of subcutaneous tumors after intravenous administration of SPN23-SiO_2-RGD or SPN23-SiO_2-PEG for 0, 8 and 24 h, respectively. The representative PA maximum imaging projection (MIP) images with axial view for the tumors of SPN23-SiO_2-RGD or SPN23-SiO_2-PEG-injected mice. Reprinted with permission from Ref. [131], copyright 2017, Elsevier Inc. All rights reserved.

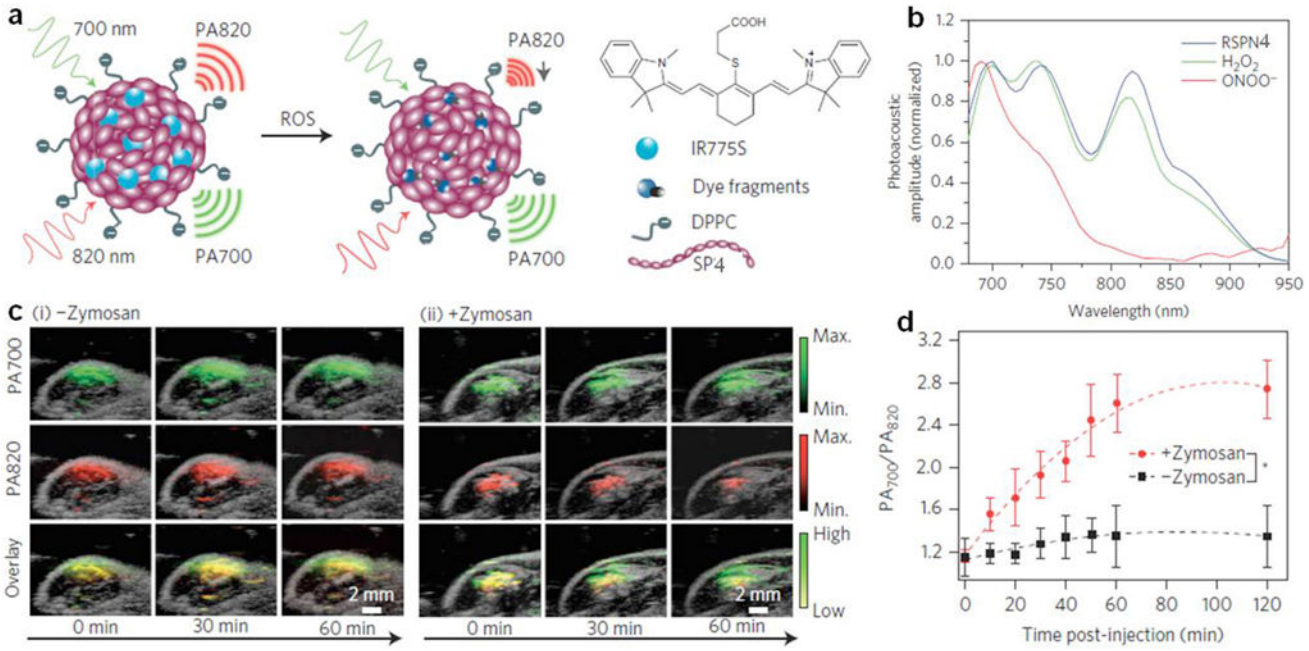

Fig. 10.

(a) Proposed ROS sensing mechanism. (b) Representative PA spectra of RSPN4 in the absence and presence of ROS. (c) PA/ultrasound overlaid images of the saline-treated (i) and zymosan-treated (ii) regions in the thigh of living mice. RSPN4 was intramuscularly injected into the thigh 20 min after zymosan treatment. (d) Ratio of PA amplitude at 700 nm to that at 820 nm (PA_{700}/PA_{820}) as a function of time post-injection of RSPN4. Reprinted with permission from Ref. [123], copyright 2014, Nature Publishing Group.

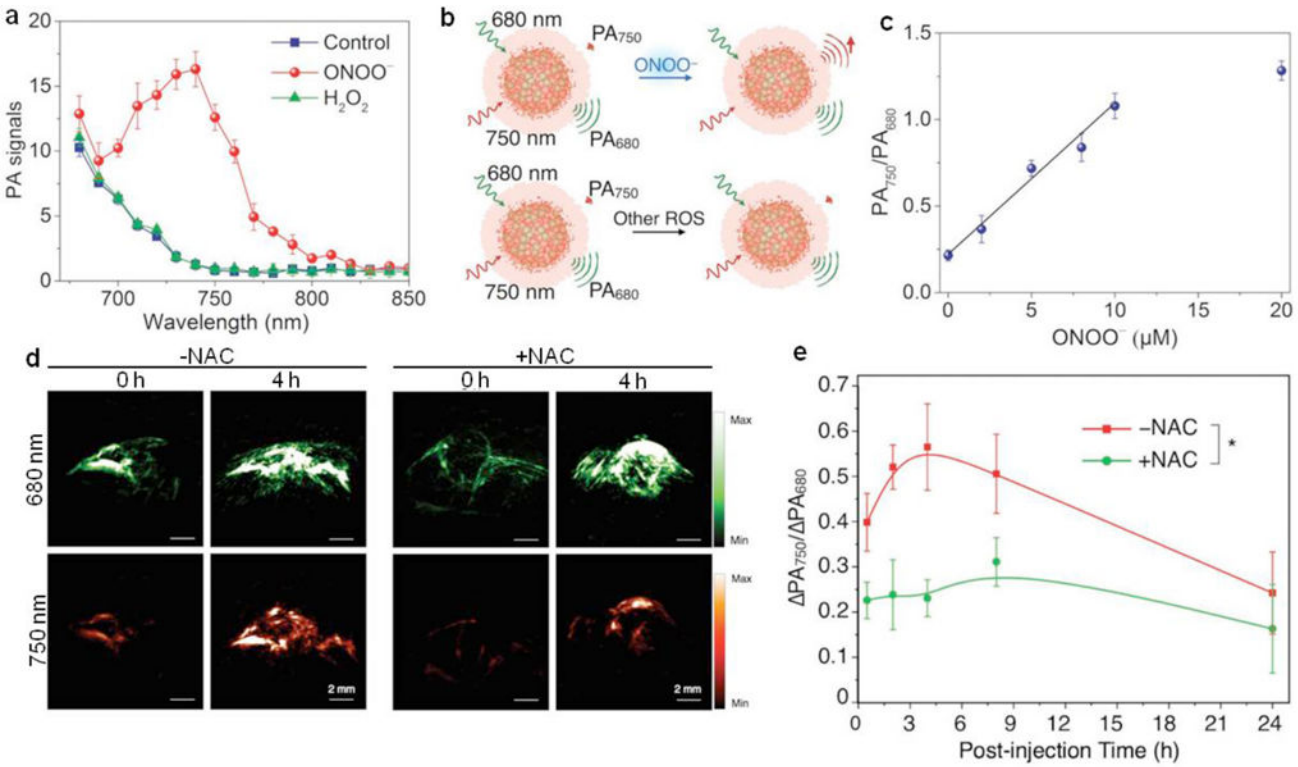

Fig. 11.

(a) PA spectra of SON5 before and after addition of $ONOO^-$ or H_2O_2. (b) Schematic illustration of PA responses of SON5 toward $ONOO^-$ and other ROS. (c) PA_{750}/PA_{680} of SON5 as a function of the $ONOO^-$ concentration. (d) PA images of subcutaneous 4T1 xenograft tumors of NAC-pretreated and untreated living mice after intravenous administration of SON5. (e) The ratiometric PA signals ($\Delta PA_{750}/\Delta PA_{680}$) as a function of post-injection time of SON5 in NAC-pretreated or untreated living mice. Reprinted with permission from Ref. [136], copyright 2017, WILEY-VCH Verlag GmbH & Co. KGaA, Weinheim.

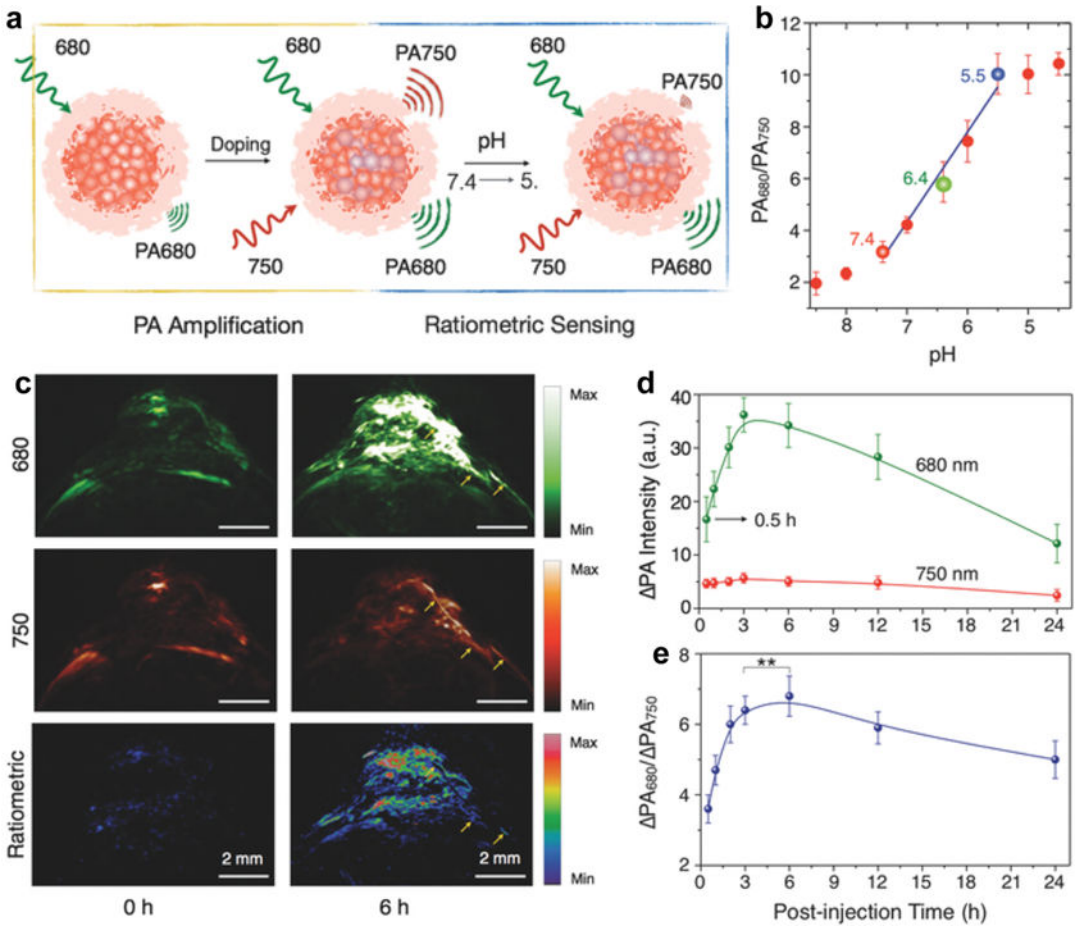

Fig. 12.

(a) Schematic illustration of doping-induced PA amplification and pH-sensing mechanism. (b) Quantification of the ratiometric PA signal (PA_{680}/PA_{750}) of $SON7_{50}$ at different pH. The blue line represents linear fitting from pH = 7.4 to 5.5. (c) PA and ratiometric images ($\Delta PA_{680}/\Delta PA_{750}$) of a subcutaneous HeLa tumor in a nude mouse before and at 6 h after intravenous administration of $SON7_{50}$. The representative PA MIP images with axial view are demonstrated. The yellow arrows indicate one of the blood vessels of the tumor. (d) Quantification of the PA intensity increment at 680 nm and 750 nm. (e) The ratiometric PA signal ($\Delta PA_{680}/\Delta PA_{750}$) as a function of time post-injection of $SON7_{50}$. The first set of data readout was conducted at 0.5 h post-injection. The pulsed laser was tuned to 680 or 750 nm for PA imaging. Reprinted with permission from Ref. [142], copyright 2016, WILEY-VCH Verlag GmbH & Co. KGaA, Weinheim.

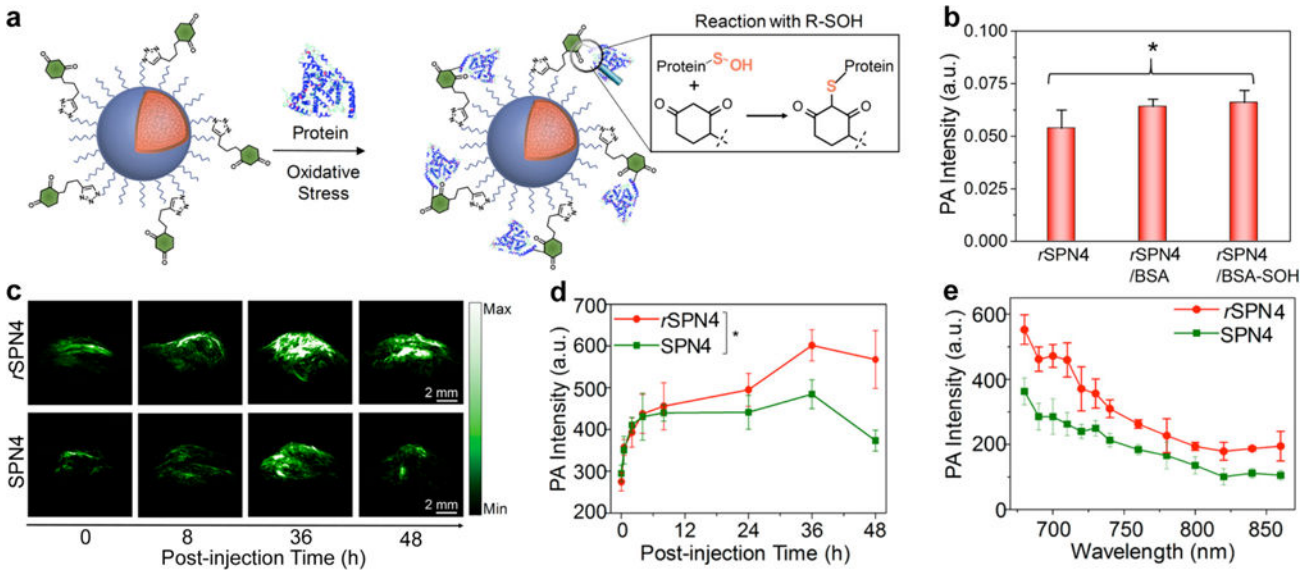

Fig. 13.

(a) Illustration of the mechanism of the specific reaction between rSPN4 and BSA-SOH. (b) PA intensities at 680 nm of rSPN4 and rSPN4 in the presence of BSA or BSA-SOH. (c) The representative PA maximum intensity projection images with axial view of tumor at representative time-points after administration of rSPN4 or SPN4 *via* tail vein injection. (d) Quantification of PA as a function of time post-injection of rSPN4 or SPN4. (e) Real-time *in vivo* PA spectra of tumor at the post-injection time of 48 h. The PA data were acquired at 680 nm. Reprinted with permission from Ref. [147], copyright 2016, American Chemical Society.

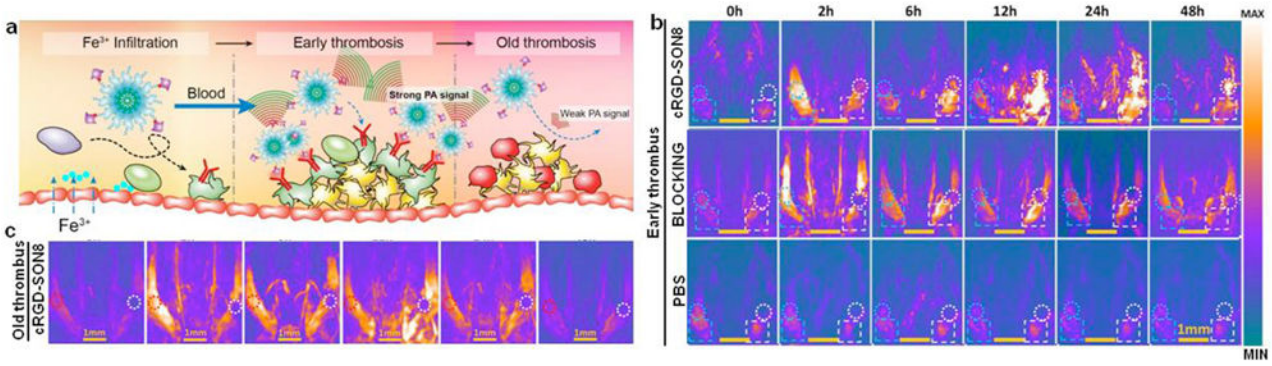

Fig. 14.

(a) Schematic illustration of the mechanism for specifically lightening early thrombus by PA imaging. (b) PA imaging of the mouse jugular veins with early thrombus of the cRGD-SON8 group, blocking group, and PBS control group at different treatment time. (c) PA imaging of old venous thrombus (3 days after injury) showing that no PA signal was enhanced in the old thrombus (region enveloped by the white dotted line) after injection of cRGD-SON8. Reprinted with permission from Ref. [149], copyright 2017, American Chemical Society.

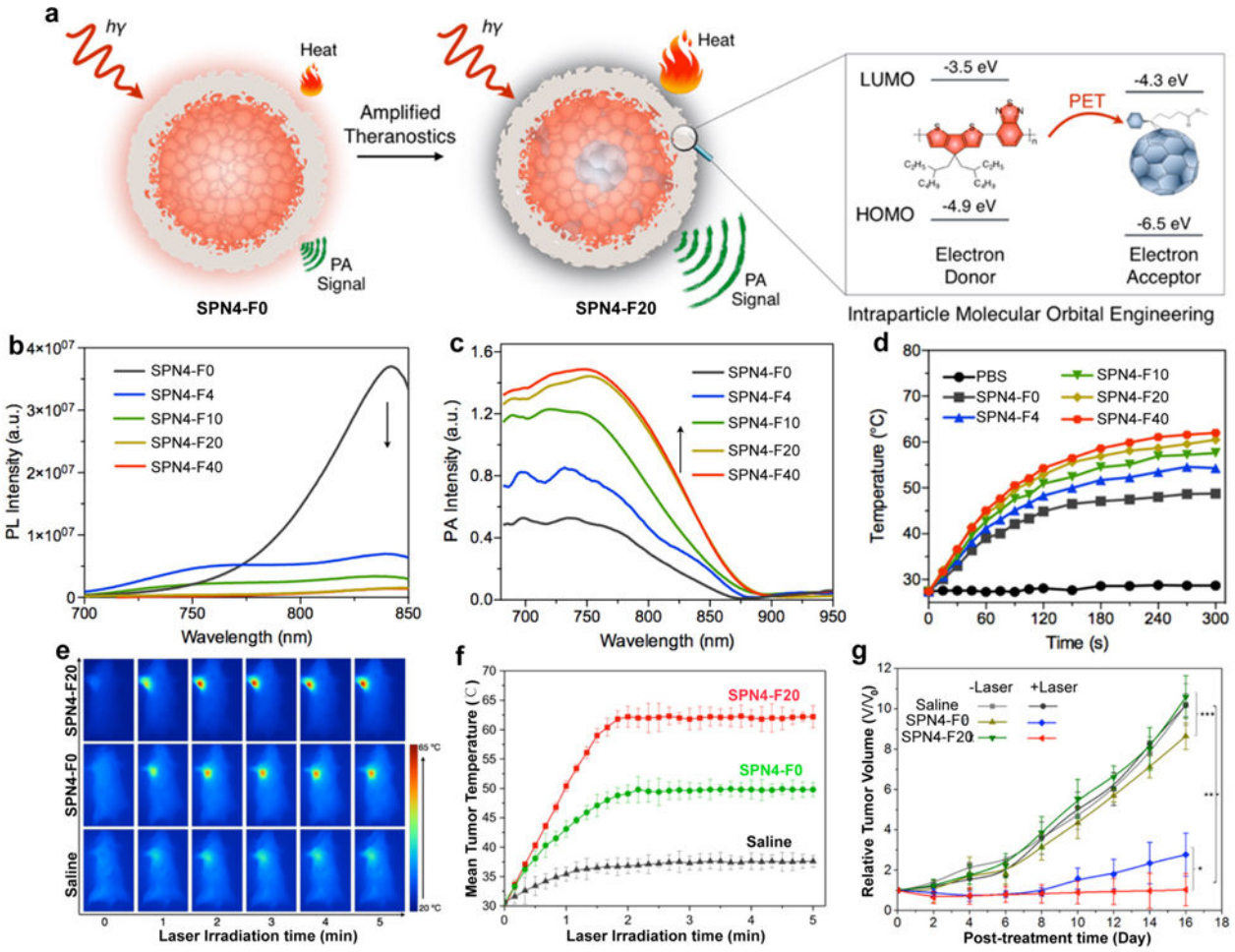

Fig. 15.

(a) Illustration of photo-induced electron transfer induced amplified theranostic SPN4-F20. The highest occupied molecular orbital (HOMO) and lowest unoccupied molecular orbital (LUMO) are −4.9 and −3.5 eV for SP4 and −6.5 and −4.3 eV for PC70BM, respectively. (b) Photoluminescene (PL) and (c) PA spectra of SPN4. The arrows indicate the decrease (b) or increase (c) of the intensities with the increased doping amount of PC70BM in SPN4. (d) The temperature of SPN4 solutions as a function of laser irradiating time at the power intensity of 0.5 W/cm^2. (e) Thermal images of 4T1 tumor-bearing mice under 808 nm laser irradiation (0.3 W/cm^2) after administration of saline, SPN4-F0, or SPN4-F20 at post-injection time of 6 h. (f) Mean tumor temperature as a function of laser irradiation time after the systemic administration of saline, SPN4-F0, or SPN4-F20 at 6 h post-injection. (g) Tumor growth curves of different groups of mice after systemic treatment with saline, SPN4-F0 or SPN4-F20 with and without laser irradiation. Reprinted with permission from Ref. [116], copyright 2016, American Chemical Society.

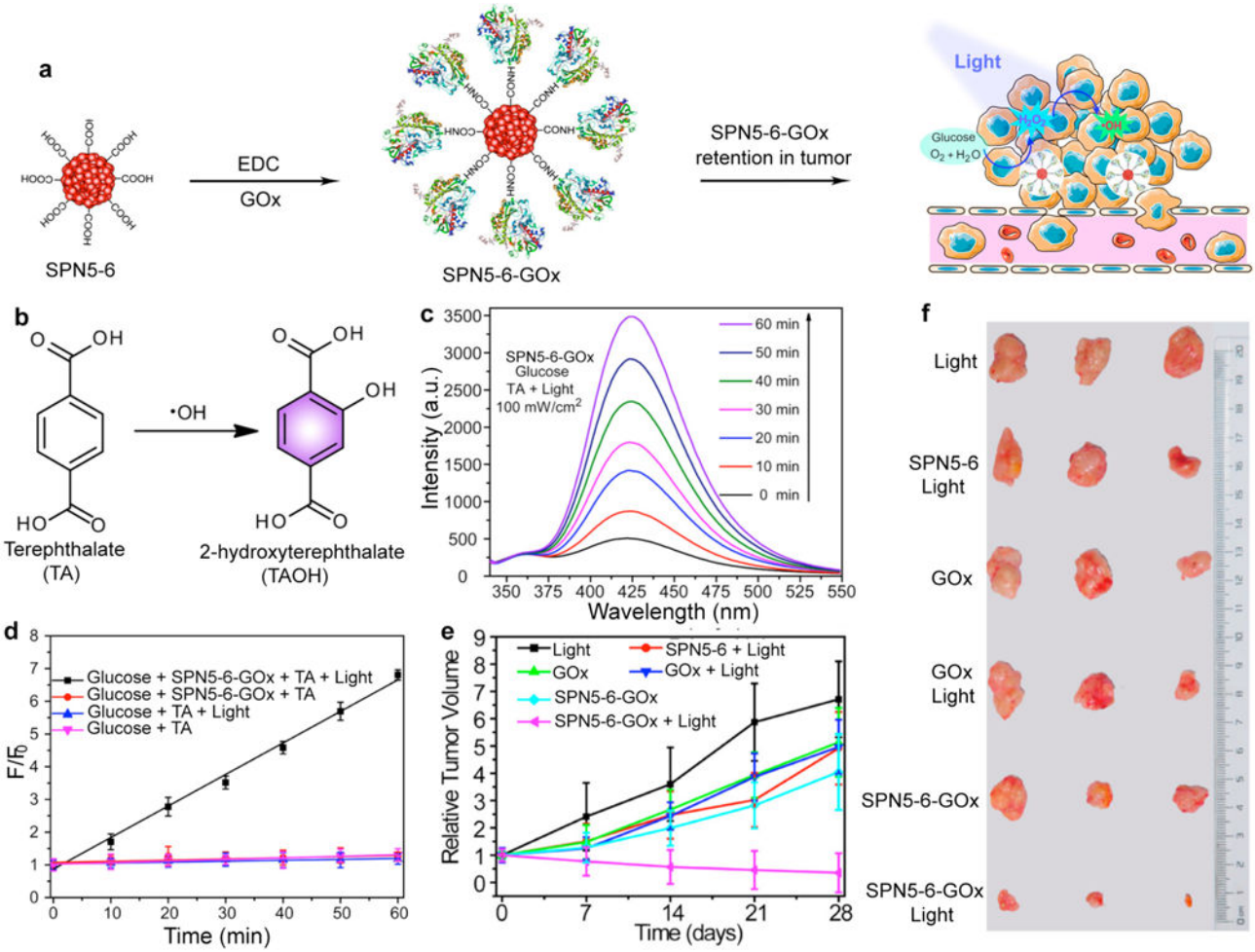

Fig. 16.

(a) Schematic illustration of SPN5-6-GOx for *in vivo* generation and photolysis of hydrogen peroxide. (b) Oxidation of TA to fluorescent TAOH by hydroxyl radicals. (c) Fluorescence spectra of TAOH induced by SPN5-6-GOx and glucose under 460 nm light irradiation for different times (0-60 min). (d) Fluorescence intensity of TAOH at 426 nm as a function of irradiation time for SPN5-6-GOx and different control treatments. F0 and F were the fluorescence intensities of the system without or with treatment, respectively. (e) Tumor growth curves in the mice receiving indicated treatments. Tumor volumes were normalized to their initial sizes. (f) Representative pictures of the tumors collected from the mice receiving indicated treatments. Reprinted with permission from Ref. [179], copyright 2017, American Chemical Society.

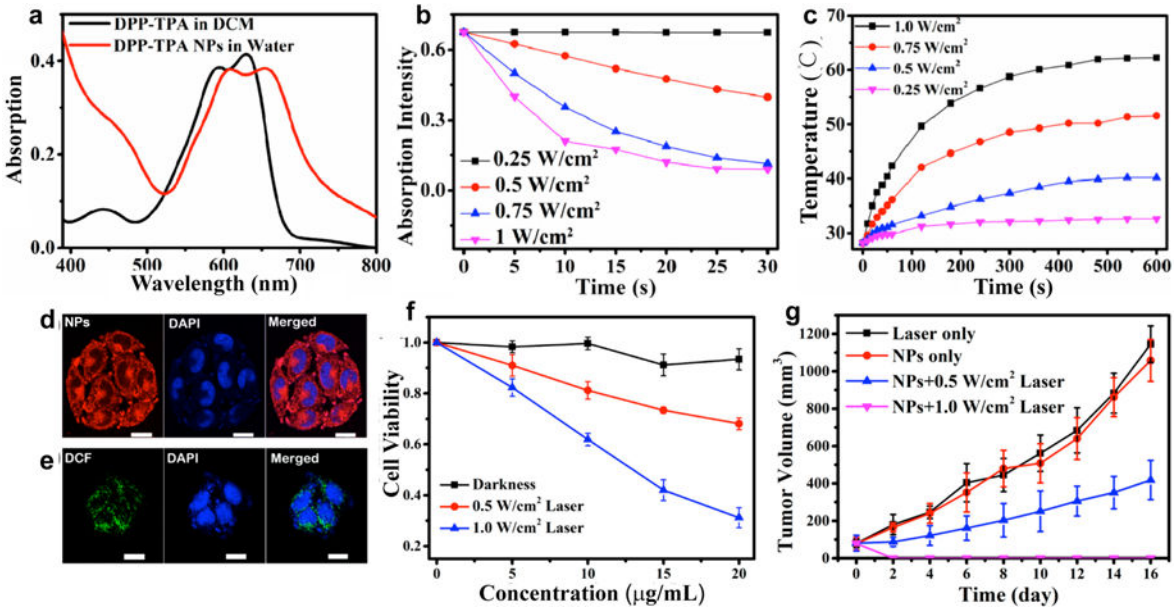

Fig. 17.

(a) UV-vis absorption spectra of SO9 in THF and SON9 in PBS. (b) Absorption intensity at 418 nm of SON9 (10^{-5} mol/L) mixed with 1,3-diphenylisobenzofuran (2×10^{-5} mol/L) in DCM over time at 660 nm laser irradiation. (c) Photothermal profiles of SON9 under different power density irradiation (660 nm). (d) Fluorescence images of SON9 in HeLa cells excited by 660 nm laser (left panel, fluorescence; middle panel, DAPI; right panel, merged images). (e) Fluorescence images of DCFH-DA in HeLa cells excited at 488 nm laser (left panel, DCF fluorescence; middle panel, DAPI; right panel, merged images). (f) The cell viability of HeLa cells after treatments with various concentrations of SON9 in different conditions. (g) Relationship between tumor volumes and time for various treatment groups. Reprinted with permission from Ref. [187], copyright 2017, American Chemical Society.

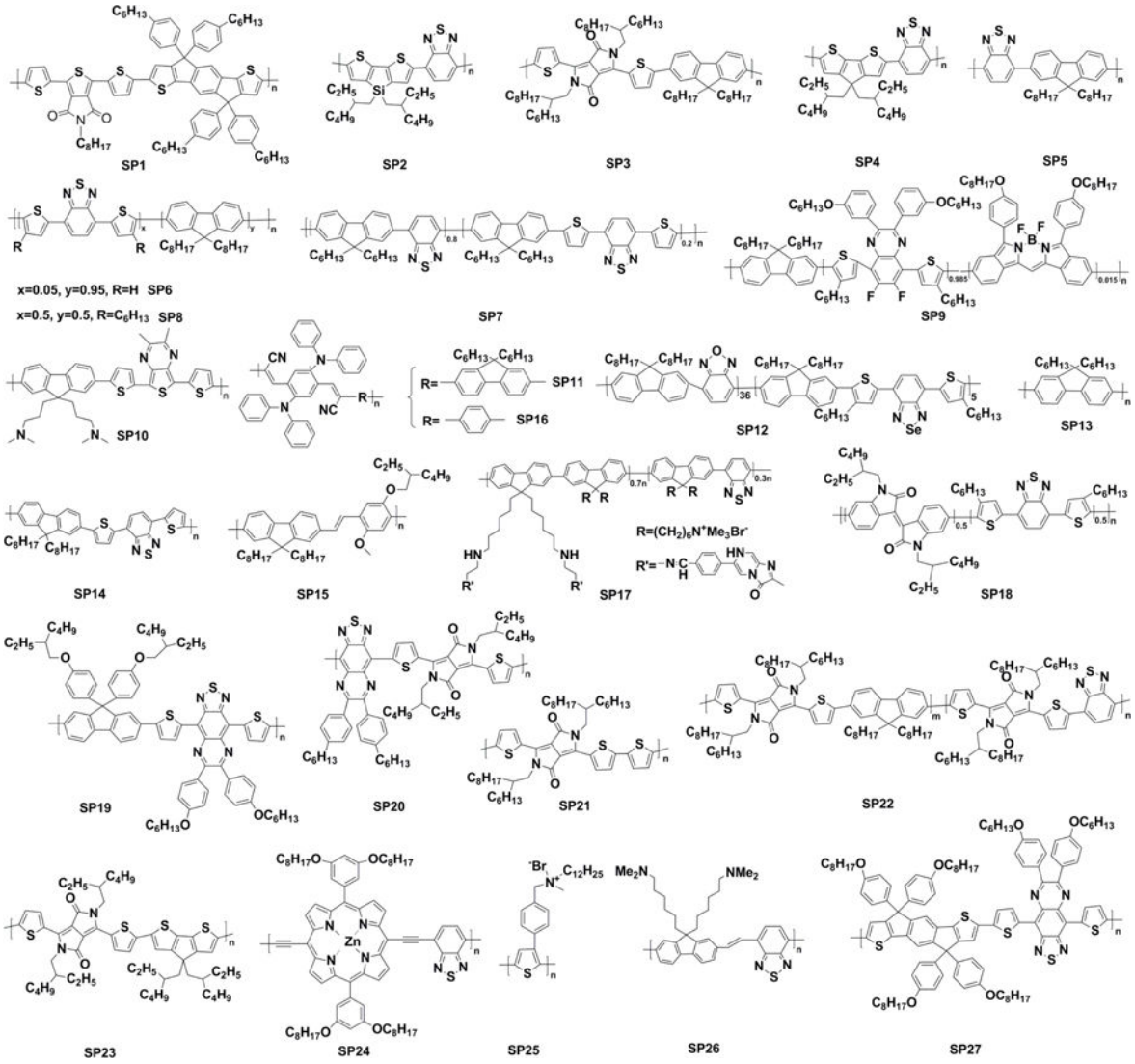

Scheme 1.

Chemical structures of SPs used for imaging and phototherapy in living mice.

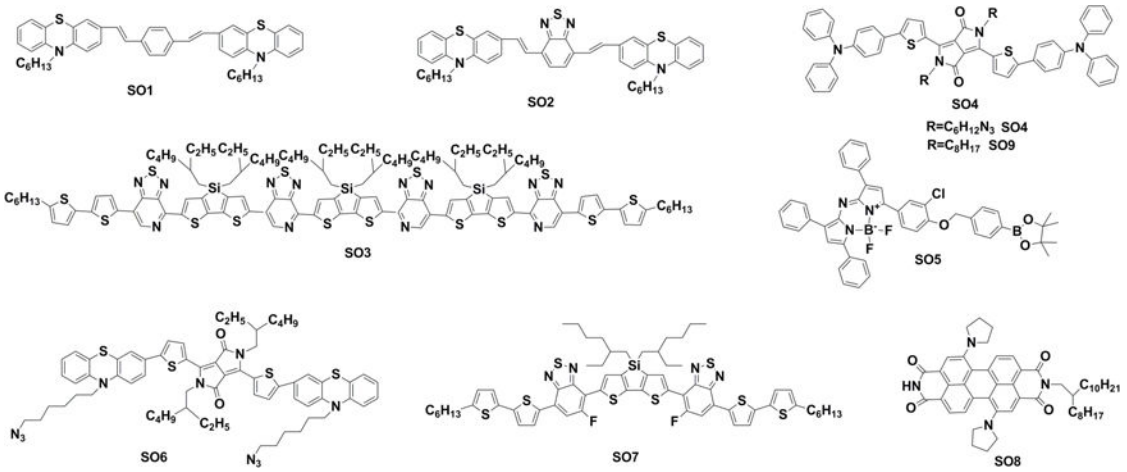

Scheme 2.

Chemical structures of SOs used for imaging and phototherapy in living mice.

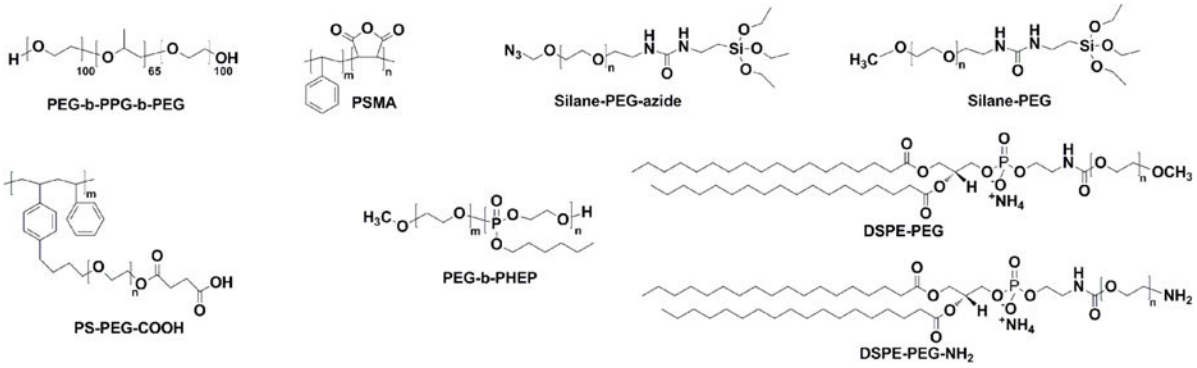

Scheme 3.

Chemical structures of amphiphilic polymers used for imaging and phototherapy in living mice.

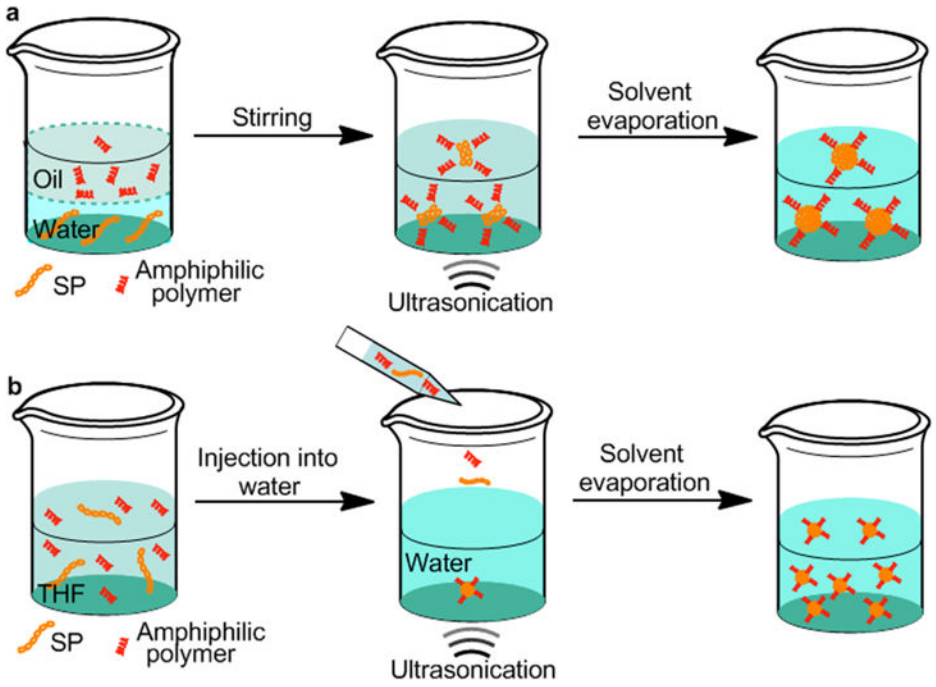

Scheme 4.

Schematic representation of mini-emulsion (a) and nanoprecipitation (b) methods for the preparation of SPNs.